* *

Black carbon aerosol reductions during COVID-19 confinement quantified by aircraft measurements over Europe

Ovid O. Krüger[1], Bruna A. Holanda[1], Sourangsu Chowdhury[2], Andrea Pozzer[2], David Walter[1], Christopher Pöhlker[1], Maria Dolores Andrés Hernández[3], John P. Burrows[3], Christiane Voigt[4,5], Jos Lelieveld[2], Johannes Quaas[6], Ulrich Pöschl[1], and Mira L. Pöhlker[1,6,7]

[1] Multiphase Chemistry Department, Max Planck Institute for Chemistry, 55128 Mainz, Germany

[2] Atmospheric Chemistry Department, Max Planck Institute for Chemistry, 55128 Mainz, Germany

[3] Institute of Environmental Physics, University of Bremen, 28359 Bremen, Germany

[4] Institute of Atmospheric Physics, Johannes Gutenberg University, 55128 Mainz, Germany

[5] Institute of Atmospheric Physics, German Aerospace Center (DLR), 82234 Oberpfaffenhofen, Germany

[6] Faculty of Physics and Earth Sciences, Leipzig Institute for Meteorology, University of Leipzig, 04103 Leipzig, Germany

[7] Experimental Aerosol and Cloud Microphysics Department, Leibniz Institute for Tropospheric Research, 04318 Leipzig, Germany

Correspondence: Mira L. Pöhlker (poehlker@tropos.de)

Abstract. The abrupt reduction in human activities during the first lockdown of the COVID-19 pandemic created unprecedented atmospheric conditions. To quantify the changes in lower tropospheric air pollution, we conducted the BLUESKY aircraft campaign and measured vertical profiles of black carbon (BC) aerosol particles over Western and Southern Europe in May and June 2020. We compared the results to similar measurements of the EMeRGe EU campaign performed in July 2017 and found that the BC mass concentrations (M_{BC}) were reduced by about 48%. For BC particle number concentrations, we found comparable reductions. Based on EMAC chemistry-transport model simulations, we found differences in meteorological conditions and flight patterns responsible for about 7% of the M_{BC} reductions. Accordingly 41% of M_{BC} reductions can be attributed to reduced anthropogenic emissions. Our results reflect the strong and immediate positive effect of changes in human activities on air quality and the atmospheric role of BC aerosols as a major air pollutant in the Anthropocene.

1 Introduction

To subdue the exponential spread of the SARS-CoV-2 (severe acute respiratory syndrome coronavirus type 2), most European countries responded with substantial cuts in mobility and economic activities. This included forced and voluntary confinements such as travel bans, home-office and relinquished travel activities (Hale et al., 2021; Quaas et al., 2021a, details on lockdown strength in Fig. A1 and section A2). Many of these behaviour modifications decreased fossil fuel combustion, a major source of atmospheric black carbon (BC) (e.g., Pöschl, 2005; Bond et al., 2013). This decrease is reflected in a roughly 30 % decreased fossil fuel demand in early 2020 (Fig. A2). That reduction is attributed to 90 % less air traffic in Europe (Schumann et al., 2021b) as well as strongly reduced road traffic (Figs. A3, A4, A5). These changes in anthropogenic emissions created unprecedented atmospheric conditions compared to the generally anthropogenic shaped continental aerosol burden (Andreae, 2007) and gave rise to the opportunity to measure airborne BC.

Several model studies use proxies like the strictness of the confinements or mobile phone data on transportation to show the impact of behavior changes on emissions (e.g., Forster et al., 2020; Le Quéré et al., 2020). Also satellite-based observations are used to track changes in trace gas concentrations, aerosol optical properties as well as cloud coverage (e.g., Quaas et al., 2021b; Schumann et al., 2021a; Li and Groß, 2021). A more accurate estimate on costs of spatial resolution is achieved with surface air pollution monitoring stations (e.g., Evangeliou et al., 2021; Petetin et al., 2020; Shi et al., 2021). All these studies have contributed to understanding the COVID-19 confinement's influence on the atmosphere and climate. Nevertheless, they fail to provide a precise quantification of air pollutants over a large spatial area with profiles of the lower tropospheric distribution. Here we present the first airborne in-situ observations of BC during the first COVID-19 lockdown in early 2020, showing a consistent data set for a large region along with the vertical distribution of BC.

We measured refractory BC mass (M_{BC}) and particle number concentrations (N_{BC}) in the lower troposphere in Western and Southern Europe (Fig. 1). The measurements were carried out with a single particle soot photometer (SP2) mounted on the HALO (High Altitude and LOng range) research aircraft. This study compares data from in-situ measurements during non-confinement conditions in July 2017 (during the EMeRGe EU campaign, Andrés Hernández et al., 2021) with those affected by reduced emissions in May and June 2020 (during the BLUESKY campaign, Voigt et al., 2022). The measurements were performed while most of the lockdown confinements were still active, however, the strictest lockdown was between the middle of March until the middle of May (Fig. A1 and section A2). Here we estimate to what extent the BC reductions are due to lower emissions and to other factors such as meteorological conditions and differences in flight tracks. Therefore we modeled M_{BC} along the flight tracks with the ECHAM/MESSy Atmospheric Chemistry (EMAC) model and used the differences in the model results to adjust our in-situ data for changes not related to reduced anthropogenic emissions. We show for the measurement period in 2020 a substantial reduction in BC compared to the measurements from 2017.

The fast response on the BC burden can be explained by its relatively short atmospheric residence time, ranging from some days to a few weeks (Holanda et al., 2020; Lund et al., 2018; Bond et al., 2013). Despite its short residence time, BC absorbs
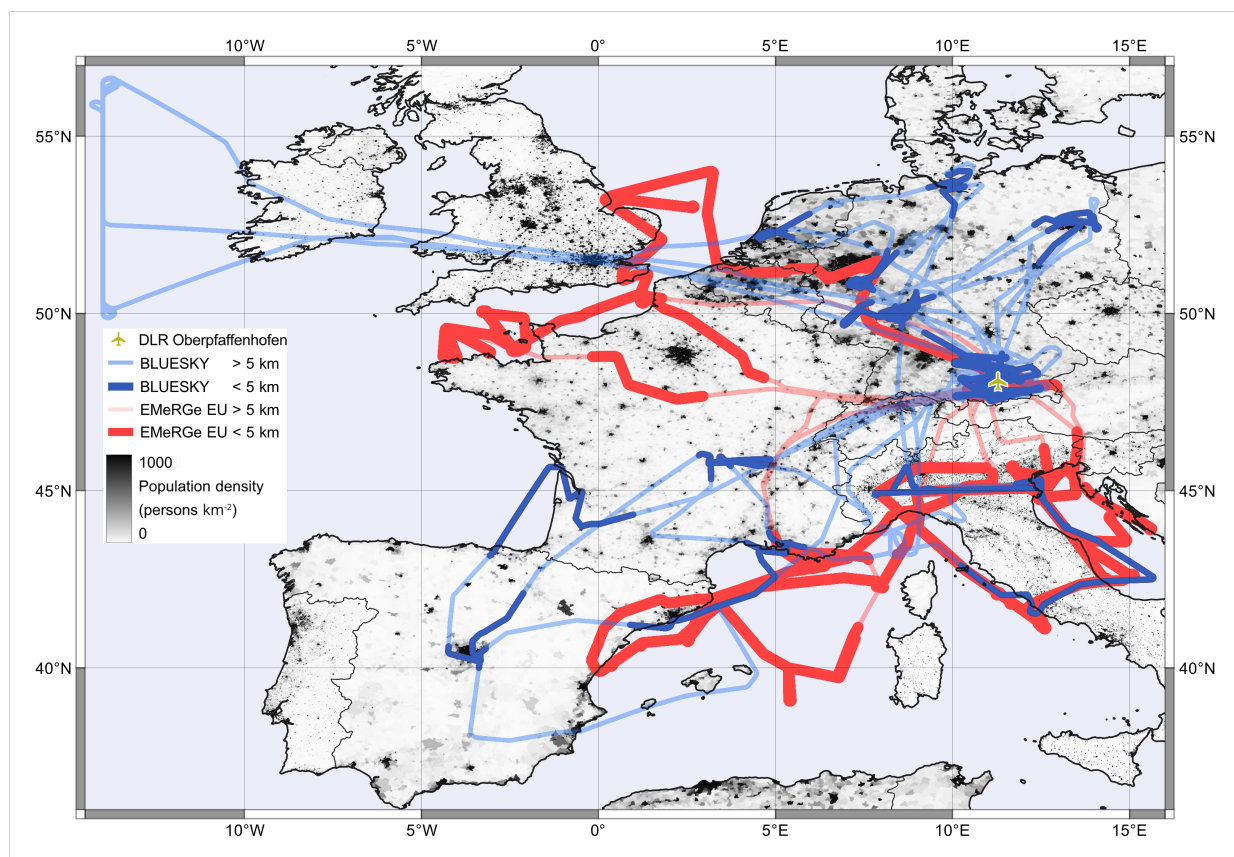
Figure 1. Flight tracks of the HALO EMeRGe EU (EM, in July 2017, Andrés Hernández et al., 2021) and BLUESKY (BS, in May and June 2020, Voigt et al., 2022) aircraft campaigns. Both campaings were conducted from the DLR airport in Oberpfaffenhofen in Southern Germany. Flight segments with altitudes below 5 km, which yielded the measurement data for this study, are highlighted in the map. The population density is for the year 2020 (CIESIN, 2018).

solar radiation which leads to strong positive radiative forcing (RF) (Ramanathan and Carmichael, 2008; Bond et al., 2013; Gustafsson and Ramanathan, 2016; Naik et al., 2021. In Press). Owing to its relatively short atmospheric residence time the BC burden response is nearly immediate to emissions changes. This immediacy makes BC an appropriate tracer for the rapid changes in anthropogenic activities and thus an important quantity in estimating the radiative effect of the 2020 confinements.

This manuscript is structured as followed, subsequent to the introduction we provide our major findings in section 2 followed by a discussion in section 3. Details about the methods and materials can be found in the appendix A. Links to corresponding sections in the appendix are provided in sections 2 and 3 where appropriate.

2 Results

The focal point of this study is the comparison between two HALO measurement campaigns, conducted over South and West Europe in 2017 and 2020 (Fig. 1 and A1). By using EMAC model simulations we quantify to what extent the pandemic-related confinements in 2020, on one hand, and other factors such as meteorology, on the other hand, influenced the observed M_{BC} reduction. In addition, the atmospheric distribution of BC and its dependency on the magnitude of emissions is analyzed. Furthermore, we examine the regional direct radiative effect of the BC reduction.

Determining the adjusted vertical distribution of the 2020 measurements (Fig. 2 d and section A7) enables us to quantify the anthropogenic emission reductions between both campaigns. Consequently, we calculated the difference between the two vertical distributions of M_{BC}, retrieved from the two initial EMAC model simulations (Fig. 2 a and b). In the following we added this difference to the 2020 measurements (section A7), to generate an adjusted vertically integrated M_{BC} burden (section A9) of $129\,\mathrm{mg\,m^{-2}}$ for 2020, whereas the actual measured burdens are $113\,\mathrm{mg\,m^{-2}}$ for 2020 and $219\,\mathrm{mg\,m^{-2}}$ for 2017. Accordingly, the difference between the adjusted M_{BC} burden for 2020 to the actual measurements from 2017 of $90\,\mathrm{mg\,m^{-2}}$ is attributable to reduced anthropogenic emissions. This value corresponds to a $41\,\%$ reduction in median M_{BC} burden.

In accordance with the analysis described above (also, section A7), we performed an evaluation of the regional sensitivity of the emission reductions. Therefore we separated our data set at a latitude of $47°N$ due to different vertical distributions and absolute concentrations North and South of that threshold (Fig 3). Beside the differences M_{BC} the threshold also represents a rough estimate of the Alps corresponding to the HALO flight tracks. South of $47°N$ the median adjusted vertically integrated M_{BC} burden is $37\,\%$ reduced whereas concentrations North of $47°N$ are $38\,\%$ lower in 2020 compared to 2017 (Fig. A7). These results are in a good agreement with the reductions of $41\,\%$ we found for all data, showing that there is only little regional sensitivity for the reported M_{BC} reductions.

Beside an emission reduction, also other factors influence the differences in measured M_{BC}. Figure 2 shows the median vertical distribution of measured and modeled M_{BC}. For the two initial model runs (Figs. 2 a and 2 b) we used identical emission inventories for the year 2014 (Hoesly et al., 2018). This approach enables us to compare our measurements with an quantity independent from anthropogenic emissions (i.e. we apply the same emissions for both campaigns) and only account for drivers other than emission reductions for differences in M_{BC}. While the 2017 measured mass burden is $4\,\%$ overestimated by the model (Fig. 2 a and TableA4), the measurements under confinement conditions are overestimated by $47\,\%$ in the model, when considering 2014 emissions (Fig. 2 b). These results demonstrate that meteorological influences, different flight patterns and differences in seasonal emissions cannot explain the observed change in lower tropospheric M_{BC}. As metric for the direct comparison of the two measurement campaigns, we use the model results to adjust our measurements. Therefore, we calculate the difference of the model results for 2017 and 2020 for each altitude bin. Overall, the difference in modeled M_{BC} between 2020 and 2017 accounts for a reduction of $7\,\%$ relative to 2017. This difference is a consequence of different flight pattern, meteorological conditions and seasonal variations in emissions.

We find a good agreement for the the shape of the vertical BC distribution for measured and modelled M_{BC} profiles. Even though the concentrations in 2020 are strongly overestimated the vertical extent is well described by the EMAC simulations (see also 2 C with reduced anthropogenic emissions). The Pearson coefficient of determination (R^2) for the vertical profiles of the observation-model comparison is 0.76 for EM and 0.90 for BS (Fig. A11). Based on the good agreement for the general vertical distribution during both campaigns, we conclude, that the shape of the vertical distribution of anthropogenic BC in the lower troposphere remains unaffected by the emission changes in 2020.

We compare the median vertical profiles in this study to simplify the heterogeneously distributed M_{BC} over Europe (Fig. 3). The vertical distribution of BC is strongly influenced by the planetary boundary layer (PBL) height, whereas its geographic pattern is more sensitive to emission hot spots like large cities or industrial areas. Elevated M_{BC} during BLUESKY were mostly confined to the PBL in good agreements with observations for Western Europe in the course of EMeRGe EU and literature (e.g., Ding et al., 2019). In Southern Europe, however, M_{BC} was stronger decoupled from the PBL and we also observed high concentrations within the lower free troposphere in 2017 and occasionally in 2020. During both campaigns, M_{BC} in Southern Europe exceeds values in Western Europe (at latitudes North of $47\,°N$). During the measurements in 2017, we also encountered mixed biomass burning and anthropogenic pollution in and above the PBL. Whereas the measurements in 2020 were not significantly influenced by biomass burning emissions (Fig. A14). The biomass burning influence was prominent in Southern Europe from $40\,°N$ and $42\,°N$ latitude (Figs. 3 a and A13). The defined BC plume between 2000 and 3500 m altitude in Southern Europe is dominated by biomass burning emissions. This biomass burning influence also caused the large discrepancies between the median and mean concentrations between 2000 m and 3500 m in figures 2 a and A7 a. An analogy can be drawn to previous studies, which reported a similar pronounced stratification of biomass burning smoke above the PBL (Holanda et al., 2020). To be less sensitive to event-like measurements, we use median values for the comparison of the two aircraft campaigns (see also section A5).

The measured values for M_{BC} in 2020 are $48\,\%$ lower, when disregarding the model-based adjustment described above. For the refractory BC particle (rBC) number concentration (N_{BC}), we also find $48\,\%$ lower concentrations (Fig. 2 e). The good agreement between M_{BC} and N_{BC}, is in accordance with the constant M_{BC} to N_{BC} ratios over its vertical distributions (Fig. A15). Also, the comparable median size distribution of the rBC particles between the two measurement campaigns, with rBC core diameters (D_{rBC}) ranging between $\sim$120 to 180 nm (Fig. A8) shows the good agreement. The larger D_{rBC} during the measurements in 2017 are likely due to influences of biomass burning smoke which tend to have larger D_{rBC} compared to urban emissions (e.g., Schwarz et al., 2008; Liu et al., 2014; Holanda et al., 2020). The consistent ratio between M_{BC} and N_{BC} (Fig. A15) indicates that differences in coagulation growth are unlikely to play a significant role for the vertical profiles of D_{rBC} reported here. Coagulation tends to predominately remove smaller particles and thus has a stronger impact on number concentrations than on the mass concentration (Ketzel and Berkowicz, 2004). This trend is not observable in our data (Fig. A15). Also anthropogenic BC emissions in Europe tend to get diluted before significant coagulation initiates (Vignati et al., 1999; Pohjola et al., 2003; Ketzel and Berkowicz, 2004). Beside coagulation and different sources, also size selective removal of BC cores with larger diameters by scavenging (e.g., Liu et al., 2020; Ohata et al., 2016) could play a role in the differences between
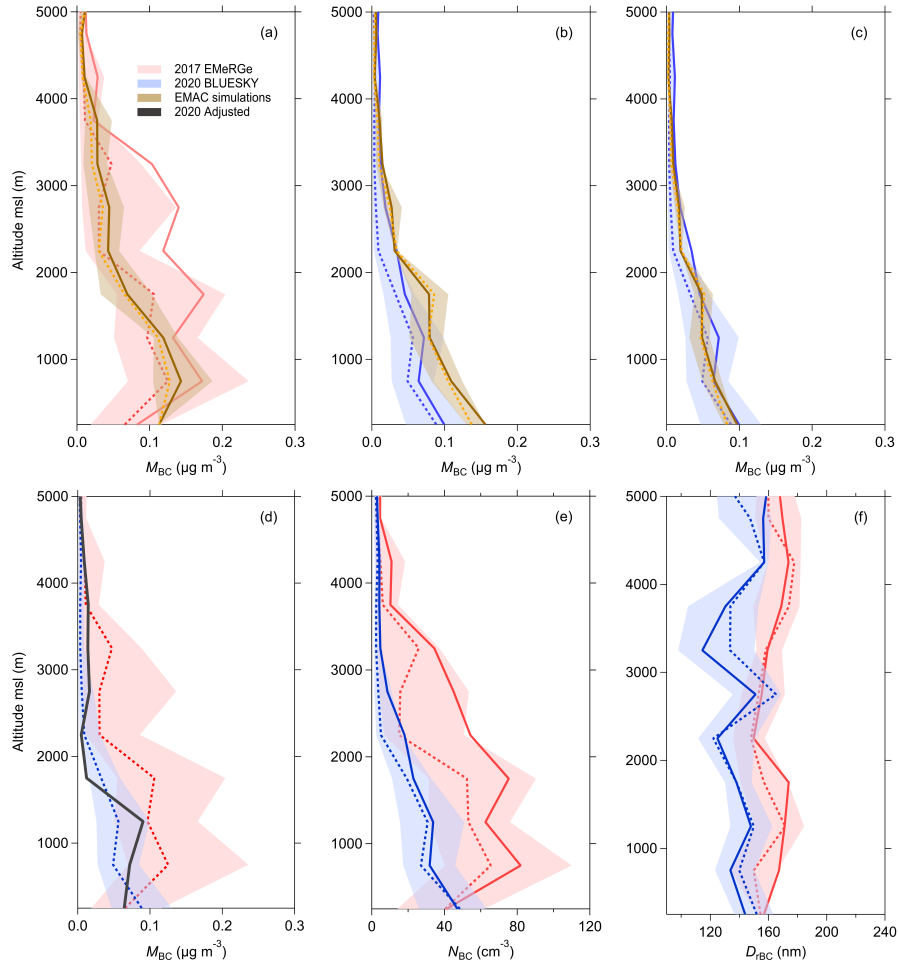
Figure 2. Vertical distributions of measured and modeled M_{BC} (a, b, c, and d). Solid lines represent arithmetic mean values, dashed lines represent median values shading marks the interquartile range. (a) shows EM 2017 measurements and EMAC simulations with initial 2014 emission inventories. (b) shows BS 2020 measurements and EMAC simulations with initial 2014 emission inventories. (c) shows BS measurements and EMAC simulations with anthropogenic BC emission reduced by 40%. (d) shows EM and BS measurements (as also shown in panels (a) and (b)) for comparison between the two campaigns. The grey solid line shows the adjusted median M_{BC} concentration expected for BS measurements in 2020 (details see section A7). The adjusted value is based on non-confinement influences retrieved from the difference in the EMAC simulations for BS and EM with the 2014 emission inventories. It represents the expected measurement value, assuming the same meteorological and seasonal conditions for both campaigns. The difference between the medians of EM and adjusted BS represents the emission reduction. (e) shows the measured N_{BC} for EM in 2017 and BS in 2020. (f) shows the geometric mean refractory BC core diameters (D_{rBC}) for EM in 2017 and BS in 2020.

Figure 3. (a) Cross section of M_{BC} for 2017 EMeRGe EU measurements. Arithmetic mean for all data falling into a grid point of $0.2°$ latitude and $500\,\mathrm{m}$ altitude. The color scale ranges from 0 to $0.3\,\mu\mathrm{g/m}^3$. Means exceeding this range are shown in red. (b) as (a) but for the 2020 BLUESKY measurements. The grey shading is the mean terrain height below flight track and the grey solid line shows the planetary boundary layer height below flight track (details in section A6).

2017 and 2020. However there are no significant differences in precipitation in the summer months in Europe. Furthermore the range for D_{rBC} agrees with literature values for urban emissions (e.g., Schwarz et al., 2008; Liu et al., 2014).

To estimate the effect the reductions have on Earth's radiative budget, we calculated the regional aerosol direct radiative effect in the measurement area. Therefore we reduced anthropogenic BC emissions in our EMAC simulation by 40% and found a cooling effect of $0.06\,\mathrm{W\,m^{-2}}$ (Fig. A9) at the top of the atmosphere (TOA). This reduction due to a reduction of anthropogenic BC emissions by 40% is as large as the global-mean BC radiative forcing, as assessed by the IPCC AR6 (Naik et al., 2021. In Press).

3   Discussion

We present the first measurement study showing the influence of the unprecedented reduction in atmospheric pollution in 2020 on BC vertical distribution. Our measurements cover a large spatial area, measured on a rather short time scale. Thus, we deliver a representative data set, showing the changes in atmospheric BC concentration. We benefit in this comparison from the large spatial coverage, measured with the same instrumentation. In addition, the vertical extent of pollutants emitted in the PBL is observed with a high accuracy. In the discussion section we compare our aircraft data with recent studies, quantifying the impact of the COVID-19 confinements with other metrics. We find a general agreement, even though most studies use 2019 or a multiyear average as reference for the comparison, while we compare two rather short periods in 2017 and 2020. We also investigate potential reasons for the reduction of atmospheric BC and other pollutants and consequently analyze data published by EUROSTAT on fossil and solid fuel demand.

The 41% reduced M_{BC} we find, exceeds the mean value for Europe (11%) reported by Evangeliou et al. (2021). Nevertheless, our results fall within the reported range from 42% to 8% for Southern and Western Europe. Also studies with stronger regional focus agree well with our results. Moreda-Piñeiro et al. (2021) found for the Southwest Atlantic region of Spain, BC reductions between 29 to 51%. Beside BC, also other atmospheric constituents were found to be reduced during the 2020 confinements. For the Po Valley, Lonati and Riva (2021) found benzene reduced by roughly 40% in May 2020. Benzene is a volatile organic compound (VOC) primarily emitted by road traffic and in good correlation with anthropogenic BC emissions (Wren et al., 2018). Petetin et al. (2020) found NO_2, as another traffic-related pollutant, decreased between 41 and 55% in Spain. By combining satellite and surface in-situ measurements with numeric modeling, Venter et al. (2020) found fine particulate matter (PM2.5) reduced by 31%. Apart from measurements, also proxy data are used to quantify the effect of the confinements on the atmosphere. Forster et al. (2020) shows globally a decrease in BC of up to 22% for the lockdown period and around 15% in May 2020. When only considering the countries probed in our measurement flights, the reduction is 40% in May and 20% in June 2020. These literature values, based on mobility data from Google and Apple, agree well with our measurements. All of the above-mentioned studies, analyzing the reductions in traffic related pollutants and proxies, are in a similar range as our results.

Less traffic is identified as the driving force for improved air quality in 2020 (Le Quéré et al., 2020). This is reinforced by the drop in fossil fuel demand during the confinements in 2020 (Figs. A2, A3, A4, A5). For May 2020, fossil fuel demand was 30% below the 2017 level (Fig. A2). We found the largest reduction in aircraft fuel demand with 75% (Fig. A5). For road traffic fuels, the decrease is roughly 20% (Diesel -18%, Fig. A3 and gasoline -32%, Fig. A4). Other than gasoline, Diesel is widely used in the transportation sector and thus the impact of the confinements in 2020 is relatively smaller. On German highways, heavy goods traffic was reduced around 25 % compared to a more than 50 % reduction in passenger cars (Goecke et al., 2020). Studies found large differences in real-world emission factors between Diesel and gasoline vehicles as well as passenger and heavy goods vehicles (Ban-Weiss et al., 2008, 2009; Wiesner et al., 2021; Peitzmeier et al., 2017), however, a source apportionment and thus a quantification of the single sources impacts on the M_{BC} reductions in 2020 is not possible based on our measurement data. The higher decrease in gasoline and aircraft fuels demand can be attributed to the drop in passenger traffic, due to travel bans, home-office, and relinquished traveling activities.

Beside reduced emissions due to the COVID-19 confinements, other emission reductions took place between the two measurement campaigns. The total consumption of solid fuels (i.e. all common coal products, details in section A11) in 2020 was around 42% below the corresponding value for 2017 (A6). However, solid fossil fuel, only accounts for a small fraction (3%) of the BC emissions from power generation (McDuffie et al., 2020). Accordingly, reductions in solid fossil fuel combustion for power generation have only little influence ($< 1\%$) on the absolute M_{BC} burden. Due to higher emission standards there are multi-year declines of the BC burden reported for the Northern Hemisphere (e.e., Singh et al., 2018; Querol et al., 2013; Kutzner et al., 2018). Based on surface measurement stations Kutzner et al. (2018) found an annual reduction between 1 and 3% for German urban background and rural sites in the period between 2005 until 2014. At traffic sites the annual reduction was as high as 5%. For a kerbside station in London, Singh et al. (2018) found up to 8% annual reduction in BC, whereas the reduction at rural and remote sites was as little as 0.6%. Querol et al. (2013) obtains similar results for Spain with a high BC reduction in urban areas and little to statistically insignificant reductions in rural regions. The BC concentrations in our study falls within the range reported by Querol et al. (2013) for remote and rural sites in Spain. It has to be noted that BC concentrations show both a strong vertical gradient and a geographic pattern, highly sensitive to emission hot spots like traffic sites, domestic combustion sources or industrial areas. Thus the median vertical profiles shall be understood as lower tropospheric background concentrations with an anticipated annual reduction in the range of rural and urban background concentrations. Hence, around 3 to 9% of the reduction we found should be attributed to long-term trends in emission reductions.

The local top of the atmosphere direct radiative effect of BC over continental Europe is considerably small, due to the low surface albedo and relatively low BC concentrations (Heald et al., 2014). Due to BC's ability to absorb solar radiation the reduced emissions show a net warming effect in the lower troposphere, by increasing the incoming radiation. However, there is a change of sign at pressure levels below 700 ($\backsim 3000\,\mathrm{m}$) resulting in an overall cooling effect at the top of the atmosphere. Nevertheless, to get a full picture of the atmospheric response to the unprecedented atmospheric situation during the COVID-19 pandemic, more sophisticated studies are needed at this point. In particular the long-range transport of anthropogenic pollutants to remote regions like higher latitudes, where its climate impact is amplified by a high surface albedo and an increased ice

melting due to deposition of atmospheric BC on snow and ice will be of interest. Also, research on the long- and short-term radiative effects in combination with other relevant species will be very valuable for atmospheric science and policy makers. For these studies we present a good estimate for the near immediate response of M_{BC} in the area of Southern and Western Europe. Furthermore, we show that proxy data as used by Forster et al. (2020) or EUROSTAT data can serve well for the improvement and the definition of emission inventories during the exceptional atmospheric circumstances during the pandemic.

4 Conclusions

We showed that lower tropospheric median M_{BC} was decreased by $41\,\%$ in Southern and Western Europe in 2020 compared to 2017. This reduction is attributed to two main reasons, the general decreasing trends of BC emissions in Germany and Europe accounting for 3 to $9\,\%$ and the confinement of human movement as a result the measures taken to minimize the spread of COVID-19 accounting for 32 to $38\,\%$. The effect of COVID-19 confinements on the atmospheric M_{BC} found in this study generally agrees with earlier studies using ground based and proxy data to estimate the confinement's effect. In addition to earlier studies, we present the first measurement results of airborne BC in 2020. We provide a consistent data set for a large spatial area and the vertical extent of M_{BC} and N_{BC}.

Our results confirm the near immediate atmospheric response of M_{BC} and N_{BC} to anthropogenic activities. Reduced mobility drives the BC reductions in the lower troposphere. Some of these changes in mobility, such as reduced road and air traffic due to home-office and video conferences, should be sustained into working culture. Model studies using our results can quantify the positive effects on public health and the atmosphere due to reductions in air pollution. Our study extends current knowledge about the distribution of pollutants in the atmosphere. It demonstrates that the impact of measures, which improve air quality, also influence climate. It thereby contributes to one of the most important challenges of this century, namely how to mitigate climate change.

Data availability. The data set for the vertical distribution of M_{BC} (Table A1), N_{BC} (Table A2), the rBC core size distribution (Table A3) and the vertically integrated M_{BC} burden (Table A4) are provided in the supplementary material. The original data set is available in NASA Ames format under https://doi.org/10.xxxxx/x. Further data from the two HALO missions is available at the HALO database (https://halo-db. pa.op.dlr.de/). For data requests beyond the available data, please refer to the corresponding author.

Code availability. The EMAC model is available under license at https://www.messy-interface.org/.

Appendix A: Materials and Methods

We investigate the impact of the first COVID-19 lockdown in Europe on atmospheric BC concentrations with aircraft measurements from 2017 and 2020. For a better understanding of impact-factors on BC other than emission reductions we model results of M_{BC} along the flight tracks. We used the resulting reductions to calculate the radiative influence due to lower BC emissions.

A1   Studied area

The measurement flights were carried out in Southern and Western European airspace (Fig. 1). The countries we focus on in this study are Germany, France, Spain, Italy, Netherlands, Belgium and Luxembourg. These countries are also used for the comparison of our results to other data sets and publications.

From 10 until 28 July 2017 the Effect of Megacities on the transport and transformation of pollutants on the Regional and Global scales (EMeRGe EU) was investigated in Europe (Andrés Hernández et al., 2021). The focus of EMeRGe EU determined the flight tracks, to be in the lower troposphere, where anthropogenic pollution is most abundant. The flights were performed predominantly up- and down-wind of dense populated regions.

We compare the results of EMeRGe EU to BLUESKY including the CAFE EU project (Chemistry of the Atmosphere: Field Experiment in Europe), from 23 May until 09 June 2020 (Voigt et al., 2022). The central point during BLUESKY was to investigate the effects of the COVID-19 confinements on the atmosphere. This included measurements of urban pollution in the lower troposphere, but also effects of reduced air traffic. Therefore, some measurements were performed in passenger aircraft cruising altitudes in the upper troposphere and lowermost stratosphere (Schlager et al. 2021 in prep.).

The two compared HALO aircraft campaigns have beside the well comparable studied area also some important differences. A major difference, which is also apparent in the vertical distributions of M_{BC} (e.g., Figs. 2, 3 and A7), is that during BLUESKY in 2020 low air traffic volume allowed us to perform more near surface measurement flights. These measurements also include manoeuvres referred as low approaches (Voigt et al., 2022), i.e. a landing manoeuvre without ground contact followed by a take off. This manoeuvre enabled us to perform more measurements within the PBL during BLUESKY compared to EMeRGe EU in 2017, when high air traffic volume inhibited these low approaches. We later account for these differences in the flight pattern with the EMAC model simulations (sections A4 and A7).

The short lifetime of BC hinders it from getting well mixed in the free troposphere and leads to a strong vertical gradient in its concentration. An accumulation of BC can be found in the lower troposphere and especially in the PBL. On top of the PBL there is some turbulent and convective mixing taking place, introducing PBL pollutants, like BC, into the lower troposphere (Andreae et al., 2018; Schwarz et al., 2017). Moreover BC concentrations in the middle and upper troposphere are rather

driven by wildfires and long range transport (Holanda et al., 2020; Ditas et al., 2018) than by anthropogenic pollution. These properties of atmospheric BC led us to focus on the lower troposphere, up to $5000\,\mathrm{m}$ above mean sea level.

Albeit, both field campaigns have a focus on emissions from major pollution centers (MPC) in Europe, the vertical distribution we report in this study (e.g., Figs. 2 and A7) are rather representative for M_{BC} in European background conditions (Querol et al., 2013). This can be explained by the fact that large fractions of the measurement flights were performed out of the MPC outflows or in highly aged air masses which also reach remote regions in Europe. All measurement flights were performed during daytime, thus there is no diurnal influence expected in our data set.

A2 Temporal course of country response measures to COVID-19 compared to measurement period

The regional severity of the COVID-19 outbreak and thus the response by the European states was not concerted. A dynamic and scattered change in restrictions was its outcome. Nevertheless, all countries covered by our measurements experienced substantial restrictions during the COVID-19 lockdown. The responses with the largest impact on air pollution include closings of schools and workplaces, the cancellation of public events, stay-at-home requirements and relinquished restrictions on both international and internal travel (Hale et al., 2021). All these restrictions led to a drastic drop in both personal mobility as well as mobility on companies business. In Figure A1 we show the governmental response index as indicator of the confinement strengths for selected countries. The data is downloaded form the Oxford Covid-19 Government Response Tracker (https://github.com/OxCGRT/covid-policy-tracker, last access 06.07.2021) and further described in Hale et al. (2021). Beside the patchy responses of particular states and provinces, the EU imposed a comprehensive travel ban for non-EU citizens, with a drop in air-traffic as outcome. This ban was in effect form 18 March 2020 until 30 June 2020 and thus covered the whole measurement period (https://data.consilium.europa.eu/doc/document/ST-9208-2020-INIT/de/pdf).

The measurement period took place in the later lockdown period, when still many confinements were in effect and travel activities remained low.

A3 Airborne BC measurements

Both measurement campaigns were conducted with the High Altitude and LOng range (HALO) research aircraft (G550, Gulfstream, USA), a modified long-range business jet. HALO is based at the German Aerospace Center (DLR) in Oberpfaffenhofen, Germany. Near isokinetic aerosol sampling was achieved with the HALO Aerosol Submicrometer Inlet mounted on the fuselage outside of the aircraft boundary layer (Andreae et al., 2018).

The refractory black carbon (rBC) was measured with an eight-channel Single Particle Soot Photometer (SP2, Droplet Measurement Technologies, Longmont, USA). The SP2 quantifies rBC and non-absorbing particles using laser-induced incandescence and scatter signals (Stephens et al., 2003; Schwarz et al., 2006). Particles with a rBC core absorb the laser light and

evaporate. The emitted incandescence signal is linearly proportional to the mass of the rBC cores (Laborde et al., 2013). The SP2 used for this study is sensitive to rBC cores in the size range between 70 to $500\,\mathrm{nm}$ mass-equivalent diameter, assuming a density of $1.8\,\mathrm{g\,cm^{-3}}$.

The SP2 incandescence signal was calibrated at the beginning, during, and at the end of each campaign with size-selected fullerene soot particles (Alfa Aesar Lot W08A039). The scattering signal was calibrated with spherical polystyrene latex size standards (208, 244, and $288\,\mathrm{nm}$) and size selected ammonium sulfate particles using a differential mobility analyzer (Grimm Aerosol Technik, Ainring, Germany). The results of all calibrations for both campaigns agreed within their uncertainty ranges, confirming good instrument stability throughout the comparison. The uncertainty for SP2 measurements is $5\,\%$ for N_{BC} and $10\,\%$ for M_{BC} (Laborde et al., 2012). The measurement data was analysed with the Paul-Scherrer Institute (PSI) SP2 toolkit (Gysel-Beer and Corbin, 2019) and adjusted to standard temperature and pressure (STP, $T = 273.15\,\mathrm{K}$, $p = 1013.25\,\mathrm{hPa}$). Throughout the analysis we use the BC data without a correction for the lower cutoff of the SP2. Due to the large contribution of anthropogenic BC emissions on our measurements and the high uncertainty in the size distribution for diameters below the SP2 detection limit we do not fit the size distribution to a log normal distribution. Furthermore for M_{BC}, diameters below $100\,\mathrm{nm}$ do not play a significant role, regardless their potentially dominating role for N_{BC} and importance for the BC surface area (Seinfeld and Pandis, 2006; Pileci et al., 2021; Schwarz et al., 2008; Reddington et al., 2013).

A4 ECHAM/MESSy model

We used the ECHAM/MESSy Atmopheric Chemistry (EMAC) model at T63 horizontal spectral resolution (approx. $1.8° \times 1.8°$) and with 31 hybrid terrain following pressure levels up to $10\,\mathrm{hPa}$ in the lower stratosphere (Jöckel et al., 2005, 2010; Pozzer et al., 2012; Lelieveld et al., 2019). The core atmospheric model employed here is the 5th generation European Centre Hamburg (ECHAM5) general circulation model. EMAC includes multiple sub-models that represent the tropospheric and stratospheric processes and their interaction with the biosphere. We used the Modular Earth Submodel System (MESSy, v.2.54, Jöckel et al., 2010; Beer et al., 2020) to link submodels that describe emission, aerosols, atmospheric chemistry, deposition and other processes. The GMXe (Global Modal Aerosol Extension) submodel (Pringle et al., 2010) was employed to simulate the microphysical processes in aerosols and the gas/aerosol portioning. The GMXe organizes the aerosols into hydrophilic and hydrophobic modes. The hydrophilic mode encompasses aerosols in the entire size spectrum (coarse, accumulation, Aitken and nucleation), whereas the hydrophobic mode does not consider the nucleation mode. We updated the assumption in the GMXe by emitting black and organic carbon in accumulation and Aitken modes following a recent study (Paasonen et al., 2016). The gas phase and heterogeneous chemistry was simulated with the MECCA submodel (Sander et al., 2005, 2019). The ORACLE (Organic Aerosol Composition and Evolution) submodel (Tsimpidi et al., 2014, 2018) was used to simulate the atmospheric evolution and composition of the organic aerosols. The aerosol optical properties are calculated by the AEROPT (AERosol OPTical properties) submodel (Lauer et al., 2007; Pozzer et al., 2012; Dietmüller et al., 2016; Klingmüller et al., 2019), which assumes the aerosol components in each mode to be spherical, well mixed and with volume averaged refractive indices. The

radiation calculations were done with the RAD submodel (Dietmüller et al., 2016) which is equipped with logical switches for diagnostically calling the radiation schemes multiple times within one model setup for calculation radiative forcings. The S4D (Sampling in 4 Dimensions) submodel (Jöckel et al., 2010) was used to interpolate and write the model outputs, online at spatial and temporal steps of the EMeRGe EU and BLUESKY aircraft measurements. Apart from these submodels, the following MESSy submodels were enabled, AIRSEA, BIOBURN, CLOUD, CLOUDOPT, CONVEC, CVTRANS, DDEP, E5VDIFF, H2O, JVAL, LNOX, OFFEMIS, ONEMIS, ORBIT, SCAV, SEDI, SORBIT, SURFACE, TNUDGE and TROPOP. Explicit description of each of these submodels can be found in the MESSy submodel list (https://www.messy-interface.org/current/auto/messy_submodels.html).

The EMAC global simulations, nudged towards the ERA-5 meteorological re-analyses were performed for two time periods January to July 2017 and January to June 2020 to coincide with the EMeRGe EU and BLUESKY aircraft campaigns respectively. Over the past decade, EMAC model simulations of aerosols and trace gases have been extensively assessed against ground measurements and satellite retrievals (Lelieveld et al., 2007; Kerkweg et al., 2006; Lelieveld et al., 2019; Tsimpidi et al., 2018; Brühl et al., 2015; Pozzer et al., 2015; Zimmermann et al., 2020). Here, we use the monthly varying Community Emissions Data System (CEDS) anthropogenic emission inventory of 2014, Hoesly et al. (2018) at $0.5° \times 0.5°$ resolution for the primary emitted species including CO (carbon monoxide), NO_2 (oxides of nitrogen), SO_2 (sulfur dioxide), NH_3 (ammonia), BC, OC (organic carbon) and NMVOCs (non methane volatile organic compounds). Biomass burning emissions were obtained from the Global Fire Assimilation System (GFAS) inventory Kaiser et al. (2012). The emissions data were then pre-processed and vertically distributed in six emission heights following Pozzer et al. (2012). Residential and commercial fuel use was the largest emitter of BC (46934 t per year) over the region investigated in this study (Fig. 1, i.e., latitude between -5 and $16°$ and longitude between 37.5 and 54.5°), followed by emissions from land transportation (36023 t per year), power generation (22161 t per year), industrial combustion and process (17737 t per year), agricultural waste burning (1283 t per year) and air traffic (0.4067 t per year). For comparisons with the EMeRGe EU and BLUESKY aircraft measurements, BC concentration was diagnosed along the aircraft routes. A sensitivity model simulation was performed by reducing anthropogenic BC emissions from all sectors by 40% to compare with the BLUESKY observations.

A5   EMAC model evaluation

Beside the comparison between the EMAC results for M_{BC} (Fig. A11), we also compare the modeled and observed ambient temperature as an independent variable (Fig. A12). The R^2 for the ambient temperature observation-model comparison is close to unity, indicating a successful nudging of synoptic variables and that the meteorological conditions during the relevant time period are simulated adequately. Locations of peaks in M_{BC} due to biomass burning emissions during EMeRGe EU (Fig. A10a) are captured by the model, whereas concentrations are underestimated (Figs. A11, A7a and A10a). The median for the $500\,m$ bins, however, turns out to be robust against these outliers (R^2 of 0.76 with a median absolute deviation (MAD) of $0.12\,\mu g/m^3$ for EM and $R^2 = 0.90$, MAD $= 0.07\,\mu g/m^3$ for BS). Whereas the average for the vertical profiles are more sensitive to peak

concentrations, leading to a significantly smaller $R^2 = 0.43$ with a high standard deviation (STD) of $0.57\,\mu g/m^3$ for EMeRGe

330 EU. For BLUESKY the $R^2 = 0.94$ with $STD = 0.16\,\mu g/m^3$ is slightly higher, compared to median values.

A6 Boundary layer and terrain height below flight track

To provide the planetary boundary layer height below the flight track in figures 3 and A10 we used the HYSPLIT package (Rolph et al., 2017; Stein et al., 2015, version 4, Revision 664, October 2014). We started a new backward trajectory every 60 seconds from the location and altitude of HALO.

335 The terrain height below the HALO flight track was computed with the online tool GPS visualizer based on the 1 second resolution coordinates of the HALO aircraft (https://www.gpsvisualizer.com/elevation, last access 20.02.2022).

To provide the arithmetic mean of planetary boundary layer and terrain height below the flight track shown in figures 3 and A10 we binned the data along the latitude in $0.2°$ steps. Then we calculated the arithmetic mean for each of these bins.

A7 Accounting for different flight pattern and seasonal and meteorological variability

340 The major difficulty in comparing atmospheric aerosol measurements is the strong dependence on multivariate as e.g., meteorological, regional and seasonal influence on the distribution and concentration of aerosol. This is due to (I) removal processes driven by the hydrological circle, dominated by cloud processing (Ohata et al., 2016; Liu et al., 2020). (II) The extent of the PBL, determining the concentration and vertical extent of bulk BC and other aerosol species (S. Raj et al., 2021). (III) Seasonal variations in emission types and strengths. Beside these factors, influencing the actual BC burden, also the flight tracks and the

345 emissions transportation pathways have an important influence on the measurement results.

We therefore used EMAC model simulations of M_{BC} along the flight tracks with different emission scenarios (details in section A4). First, we run the model for 2017 and 2020 with unmodified 2014 emission inventories (Hoesly et al., 2018). For the comparison we use one minute average measurement data $30\,s$ prior and $30\,s$ after each model output. In the next step we calculate the descriptive statistics for vertical bins of $500\,m$. The difference for each altitude bin between the results of the EMAC runs

350 for 2017 and 2020 is added to the 2020 measurement results to account for differences unrelated to emission changes (e.g., flight pattern, meteorology, and differences in emissions pattern as well as emissions from wildfires). The adjusted vertical profile for the 2020 measurements is then compared to the 2017 measurements to quantify the emission reductions according to equation A1.

$$BC_{red} = \frac{M_{BC2017H} - (M_{BC2020H} + (M_{BC2017M} - M_{BC2020M}))}{M_{BC2017H}} \tag{A1}$$

355 Where BC_{red} is the unit-less reduction factor in M_{BC} attributed to the COVID-19 confinements, M_{BC2017H} and M_{BC2020H} stands for HALO measurements. While the difference between the EMAC results (M_{BC2017M} and M_{BC2020M}) is the adjustment factor, introduced earlier.

A8 Vertical and latitudinal distribution of M_{BC} and N_{BC}

The vertical profiles of M_{BC}, N_{BC} (Fig. 2) and the microphysical BC properties in Figures 2 d and A8 represent the all measure-
360 ment data with the model output during the two campaigns. For the model evaluation we used only measurement data from 30 seconds prior and 30 seconds after a EMAC model output (Figs. A11 and A12). No EMAC simulations for N_{BC} were conducted. To obtain the vertical profiles the measurement and model data are concatenated in 500 m altitude bins. The statistical values given in the particular figure and table are calculated for each bin with IGOR Pro (WaveMetrics Inc. version 7.08). We calculated the arithmetic mean, also referred as mean within this study.

365 Also the log normal size distributions, given in Figures 2 D and A8, are calculated for the concatenated data in each altitude bin. We used the following function according to (Heintzenberg, 1994),

$$f(x) = \frac{A}{\sqrt{2\pi}log(\sigma)} \exp\left[-\frac{(\log(x) - \log(D_{\mathrm{g}}))^2}{2\log^2(\sigma)}\right] \tag{A2}$$

with A as a free parameter, D_{g} as mean geometric diameters and the widths (i.e. the standard deviations, σ_{g}) of the core size distributions.

370 ## A9 Vertically integrated M_{BC} burden

The vertically integrated M_{BC} burden per surface area is calculated as the integral of the median vertical M_{BC} concentration. We only considered vertical bins for the comparison where during both campaigns measurements were performed and EMAC model. Note that the M_{BC} per cubic metre in the vertical profiles is STP corrected. Thus, we scaled the altitude bins with a scaling factor (S_{P}, Table A4) based on the pressure altitude. Equation A3 shows the calculation of (S_{P}) with h_{bin} as the altitude
375 of the corresponding altitude bin in the vertical profile.

$$S_{\mathrm{P}} = \frac{1}{(1 - \frac{h_{\mathrm{bin}}}{4307.693\,96\,\mathrm{m}})^{5.2553026}} \tag{A3}$$

A10 Radiative impact of the changed M_{BC}

The radiative effect due to 40% reduction in M_{BC} is calculated with EMAC for the local radiative forcing (latitude between -5 and $16°$ and longitude between 37.5 and $54.5°$) for the months May and June. The radiative effect is the difference between one run with full aerosol emissions and one with 40% reduced anthropogenic M_{BC} emissions. The calculations are done for short wave radiation with clear sky conditions.

A11 EUROSTAT data for fossil and solid fuels

Data published by EUROSTAT is used to investigate the reductions in fossil fuel demand during the confinement period in 2020 (https://ec.europa.eu/eurostat/databrowser/view/NRG_JODI__custom_482779/default/table last access 25.01.2021). We use for figures A4, A3, A2, A5 the terminology suggested by EUROSTAT. However, to make these rather technical terms more clear we refer in section 3 to gasoline for motor spirits and aircraft fuel for kerosene. Furthermore, the difference in solid fossil fuel (which is the compilation of Hard coal including: Anthracite, Coking coal and other Bituminous coal; Brown coal including: Sub-bituminous coal and Lignite and Coal products including: Patent fuel, Coke oven coke, Gas coke, Coal tar and Brown coal briquettes https://ec.europa.eu/eurostat/statistics-explained/index.php?oldid=449721, last access 19.04.2022) demand between 2017 and 2020 is used to analyze important drivers for the BC reduction, other than the COVID-19 confinements in 2020 (https://ec.europa.eu/eurostat/databrowser/view/NRG_CB_SFF__custom_1131819/default/table?lang=en last access 08.07.2021 and https://ec.europa.eu/eurostat/databrowser/view/NRG_CB_SFFM__custom_1558586/default/table?lang=en last access 12.11.2021).

Table A1. Average and median M_{BC} from HALO observations and EMAC simulations. Values in column altitude represent centre of corresponding $500\,\text{m}$ altitude bin.

	EMeRGe EU				BLUESKY					
	Observations		EMAC		Observations		EMAC		EMAC 40 % reduced	
Altitude	Avg	Median	Avg	Median	Avg	Median	Avg	Median	Avg	Median
[m]	$[\mu g/m^3]$	$[\mu g/m^3]$	$[\mu g/m^3]$	$[\mu g/m^3]$	$[\mu g/m^3]$	$[\mu g/m^3]$	$[\mu g/m^3]$	$[\mu g/m^3]$	$[\mu g/m^3]$	$[\mu g/m^3]$
250	0.083	0.066	0.113	0.113	0.099	0.089	0.156	0.137	0.110	0.097
750	0.172	0.125	0.143	0.128	0.064	0.049	0.109	0.105	0.077	0.073
1250	0.132	0.097	0.119	0.112	0.072	0.056	0.079	0.078	0.056	0.055
1750	0.174	0.106	0.069	0.065	0.045	0.033	0.079	0.086	0.055	0.060
2250	0.119	0.030	0.043	0.030	0.034	0.009	0.031	0.034	0.022	0.024
2750	0.140	0.030	0.044	0.036	0.019	0.006	0.027	0.025	0.019	0.017
3250	0.103	0.047	0.028	0.021	0.012	0.004	0.015	0.010	0.011	0.008
3750	0.023	0.011	0.028	0.019	0.010	0.003	0.011	0.008	0.008	0.006
4250	0.029	0.009	0.010	0.008	0.011	0.005	0.004	0.003	0.003	0.002
4750	0.013	0.005	0.007	0.005	0.008	0.003	0.006	0.003	0.004	0.002

Table A2. Average and median N_{BC} from HALO observations. Values in column altitude represent centre of corresponding $500\,m$ altitude bin.

	EMeRGe EU		BLUESKY	
	Observation		Observation	
Altitude	Avg	Median	Avg	Median
[m]	[cm^{-3}]	[cm^{-3}]	[cm^{-3}]	[cm^{-3}]
250	41.1	40.3	47.1	48.5
750	81.8	65.4	31.8	27.0
1250	62.5	53.1	33.7	30.7
1750	75.3	52.3	22.9	19.3
2250	54.2	15.0	18.0	5.1
2750	45.0	15.6	8.6	3.5
3250	34.4	25.8	4.7	2.4
3750	10.2	6.0	4.1	2.4
4250	10.8	4.7	4.2	3.2
4750	4.6	2.9	3.2	2.6

Table A3. Average and median of M_{BC} microphysical properties, geometric mean diameters (D_{rBC}) and the geometric standard deviation (σ_{rBC}) of the core size distributions. Values in column altitude represent centre of corresponding $500\,m$ altitude bin.

	EMeRGe EU				BLUESKY			
	D_{rBC}		σ_{rBC}		D_{rBC}		σ_{rBC}	
Altitude	Avg	Median	Avg	Median	Avg	Median	Avg	Median
[m]	[nm]	[nm]			[nm]	[nm]		
250	157	155	2.083	2.047	144	152	2.180	2.063
750	167	150	2.006	1.966	134	140	2.268	2.108
1250	171	172	1.924	1.900	148	150	2.149	2.124
1750	174	157	1.872	1.858	138	138	2.027	1.972
2250	150	148	1.826	1.789	125	122	1.917	1.954
2750	155	153	1.749	1.714	151	165	1.866	1.907
3250	159	158	1.808	1.803	115	134	1.731	1.642
3750	169	174	1.701	1.735	130	134	1.642	1.634
4250	174	178	1.645	1.663	157	157	1.444	1.444
4750	170	160	1.447	1.463	157	148	1.392	1.405

Table A4. Vertically integrated M_{BC} burden per surface area. BLUESKY adjusted is the BLUESKY observation and the EMAC model retrieved adjustment (see section A7). Values in column altitude represent centre of corresponding $500\,\mathrm{m}$ altitude bin. Pressure altitude scaling factor calculated as described in section A9. Last row provides column sum of vertically integrated M_{BC} burden.

Altitude [m]	Pressure altitude scaling factor	EMeRGe EU Median [$\mathrm{mg\,m^{-2}}$]	BLUESKY Median [$\mathrm{mg\,m^{-2}}$]	BLUESKY Adjusted Median [$\mathrm{mg\,m^{-2}}$]
250	1.03	31.86	43.00	31.23
750	1.09	57.14	22.40	32.87
1250	1.16	41.51	24.26	38.88
1750	1.24	42.88	13.19	4.97
2250	1.32	11.48	3.49	1.89
2750	1.40	10.71	2.01	5.84
3250	1.49	15.86	1.18	4.70
3750	1.59	3.52	1.09	4.61
4250	1.70	2.75	1.36	2.67
4750	1.81	1.31	0.88	1.28
Sum		219.04	112.86	128.95
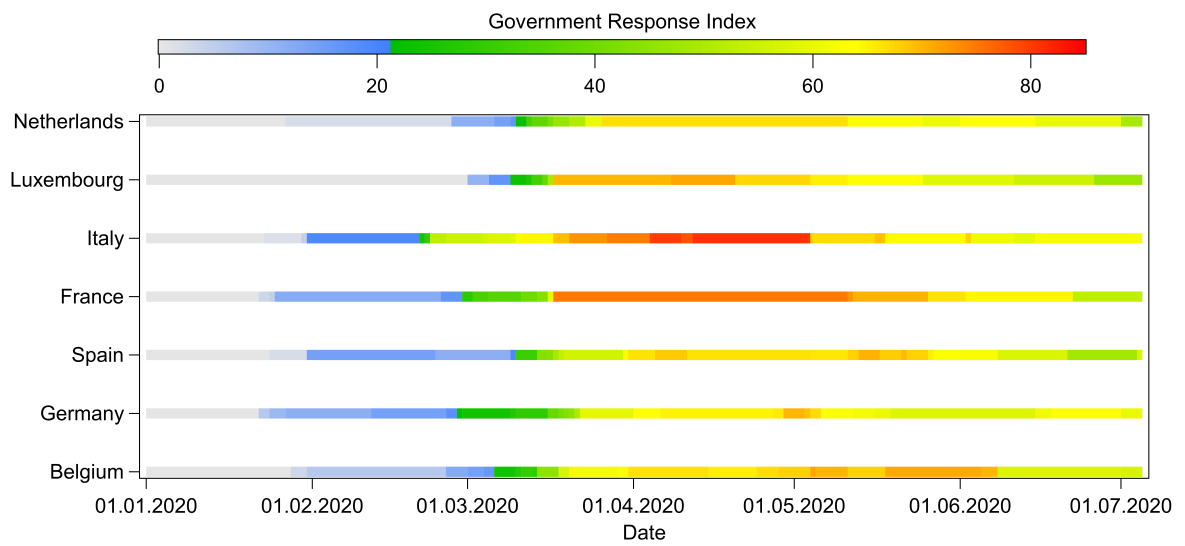
Figure A1. Temporal evolution of response on COVID-19 for selected European countries. Governmental response index data downloaded from https://github.com/OxCGRT/covid-policy-tracker/blob/3143b76020ef83072086853749c950ac0921ba47/data/timeseries/government_response_index.csv, last access 06.07.2021. Details on the governmental response index in section A2 and in Hale et al. (2021).
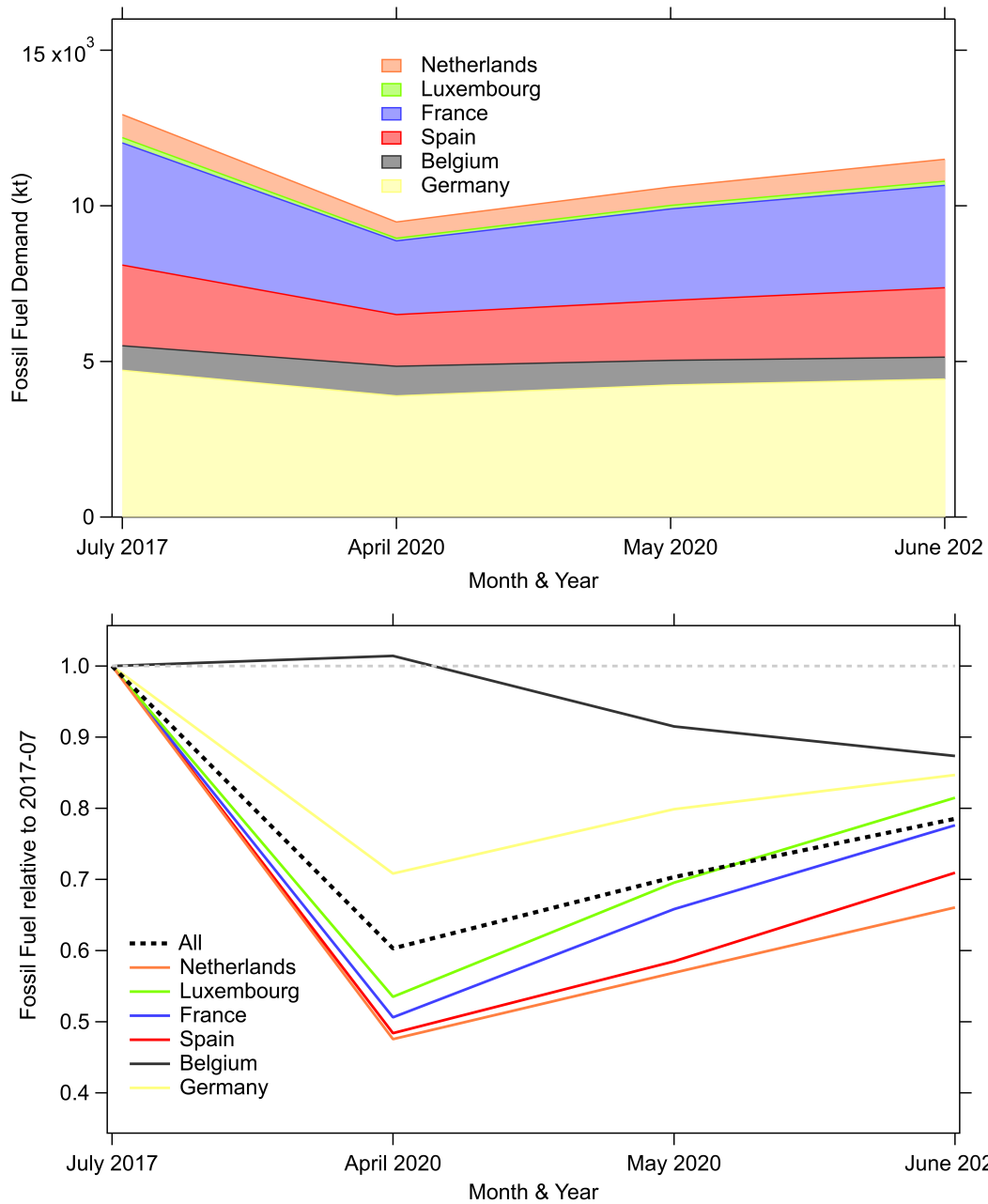
Figure A2. Cumulative EUROSTAT data for fossil fuel demand for the July 2017, April 2020, May 2020 and June 2020. The data combines demand for diesel, kerosene (aviation fuel) and motor spirit (gasoline). Data is downloaded for countries considered in this study from the EUROSTAT website with last access 08.07.2021 (https://ec.europa.eu/eurostat/databrowser/view/NRG_CB_SFF__custom_1131819/default/table).
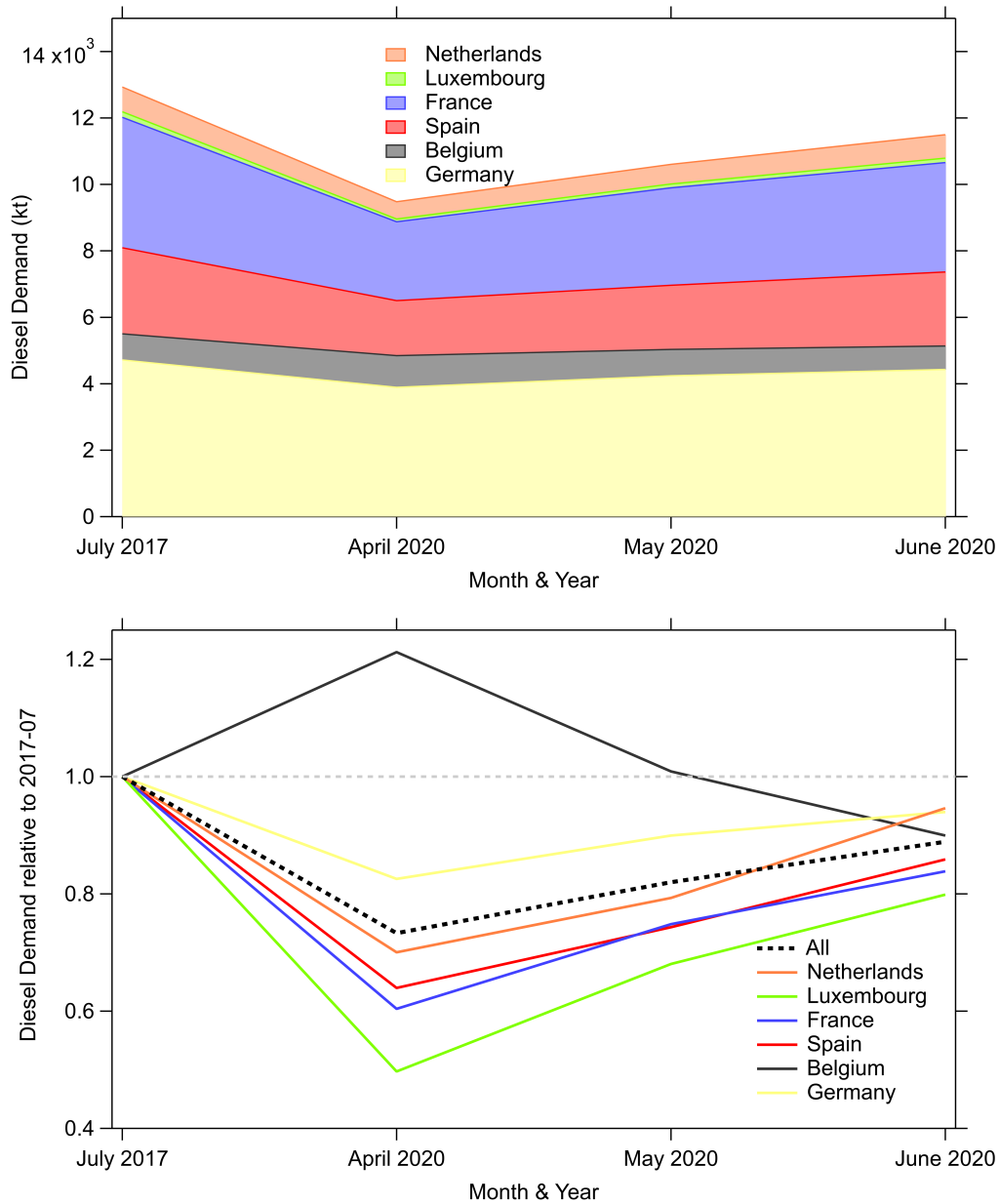
Figure A3. Cumulative EUROSTAT data for diesel demand for July 2017, April 2020, May 2020 and June 2020. Data is downloaded for countries considered in this study from the EUROSTAT website with last access 08.07.2021 (https://ec.europa.eu/eurostat/databrowser/view/ NRG_CB_SFF__custom_1131819/default/table).
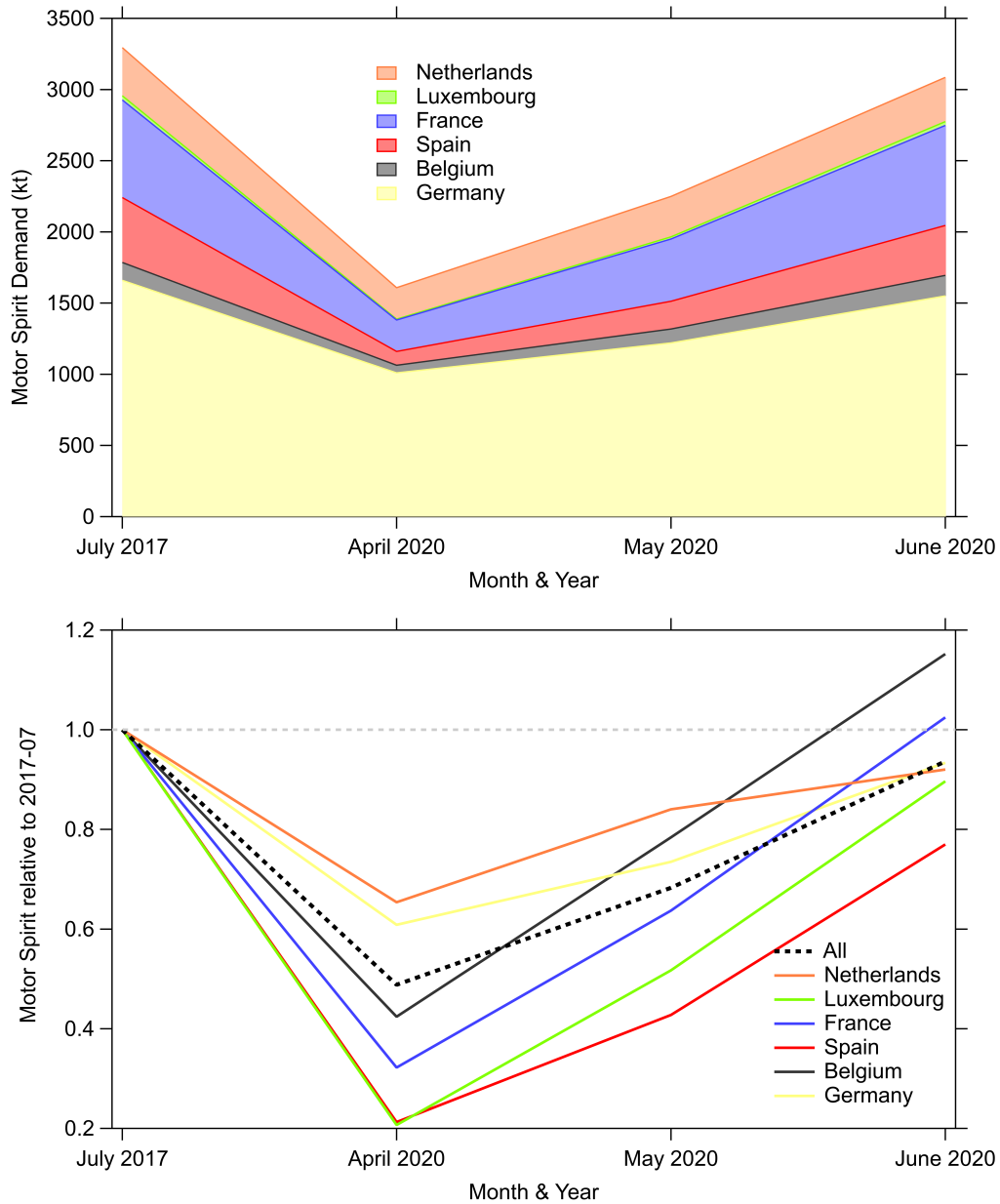
Figure A4. Cumulative EUROSTAT data for motor spirit (gasoline) demand for the July 2017, April 2020, May 2020 and June 2020. Data is downloaded for countries considered in this study from the EUROSTAT website with last access 08.07.2021 (https://ec.europa.eu/eurostat/databrowser/view/NRG_CB_SFF__custom_1131819/default/table).
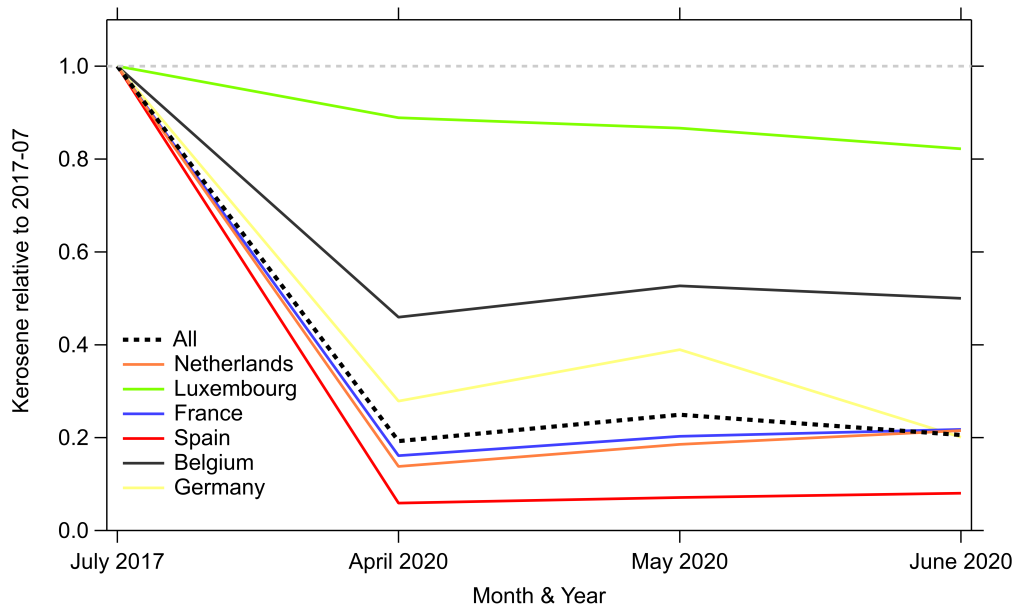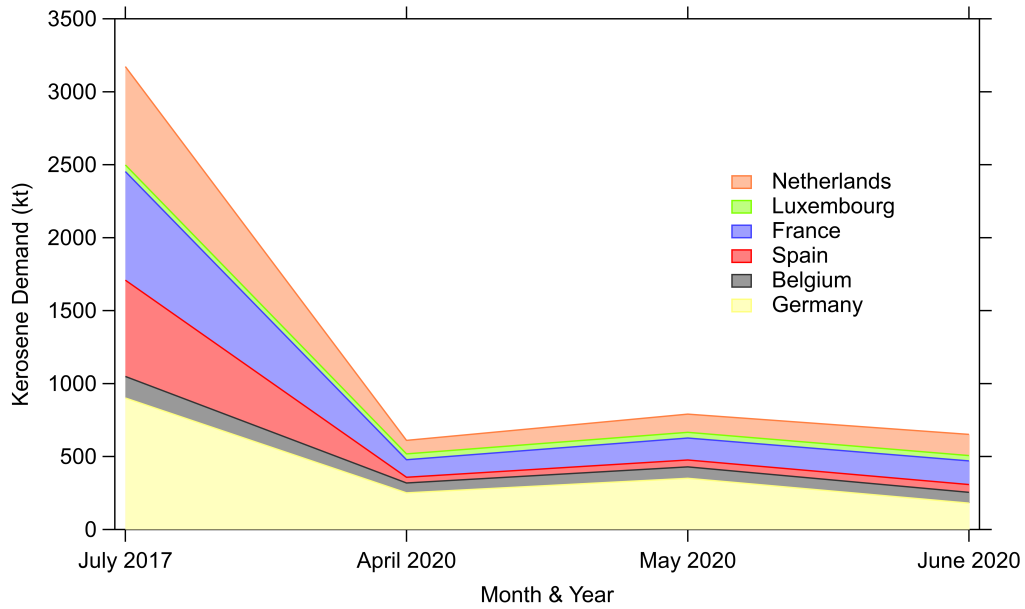
Figure A5. Cumulative EUROSTAT data for kerosene (aviation fuel) demand for the July 2017, April 2020, May 2020 and June 2020. Data is downloaded for countries considered in this study from the EUROSTAT website with last access 08.07.2021 (https://ec.europa.eu/eurostat/databrowser/view/NRG_CB_SFF__custom_1131819/default/table).
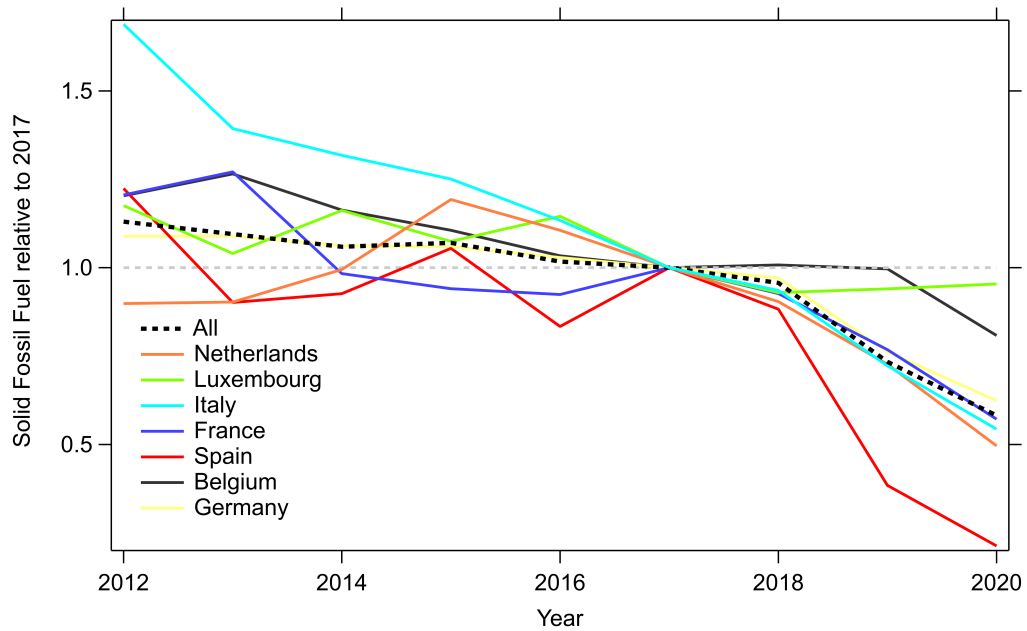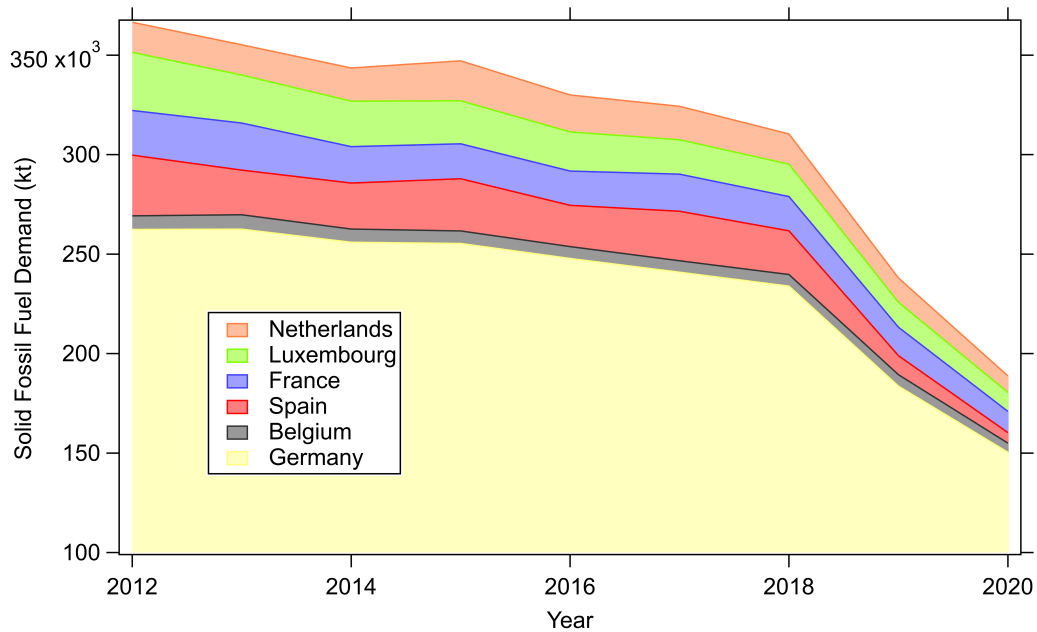
Figure A6. Cumulative EUROSTAT data for solid fossil fuel inland consumption for the years 2012 to 2020. Data is downloaded for countries considered in this study from the EUROSTAT website with last access 08.07.2021 (https://ec.europa.eu/eurostat/databrowser/view/ NRG_CB_SFF__custom_1131819/default/table).
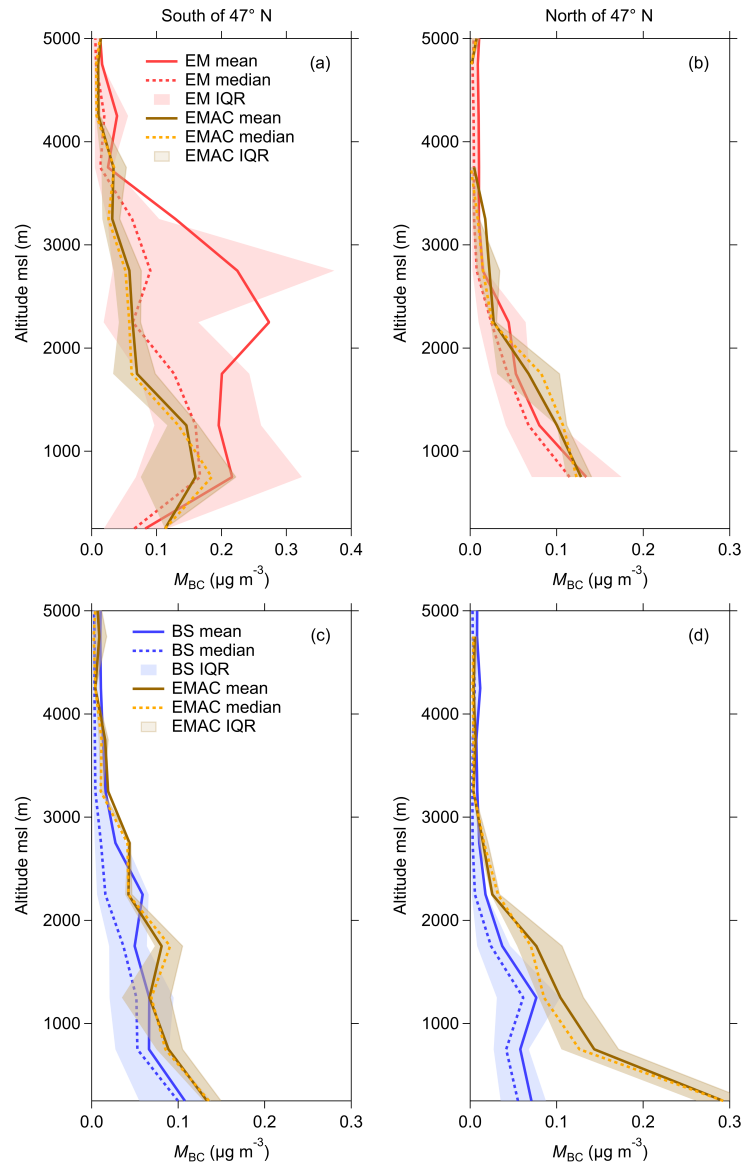
Figure A7. Vertical distribution of M_{BC} North and South of 47°N. (a) and (b) show data for EM from 2017, (c) and (d) for BS from 2020. Note that the x-axis in (a) ranges between 0 to $0.4\,\mu g/m^3$.
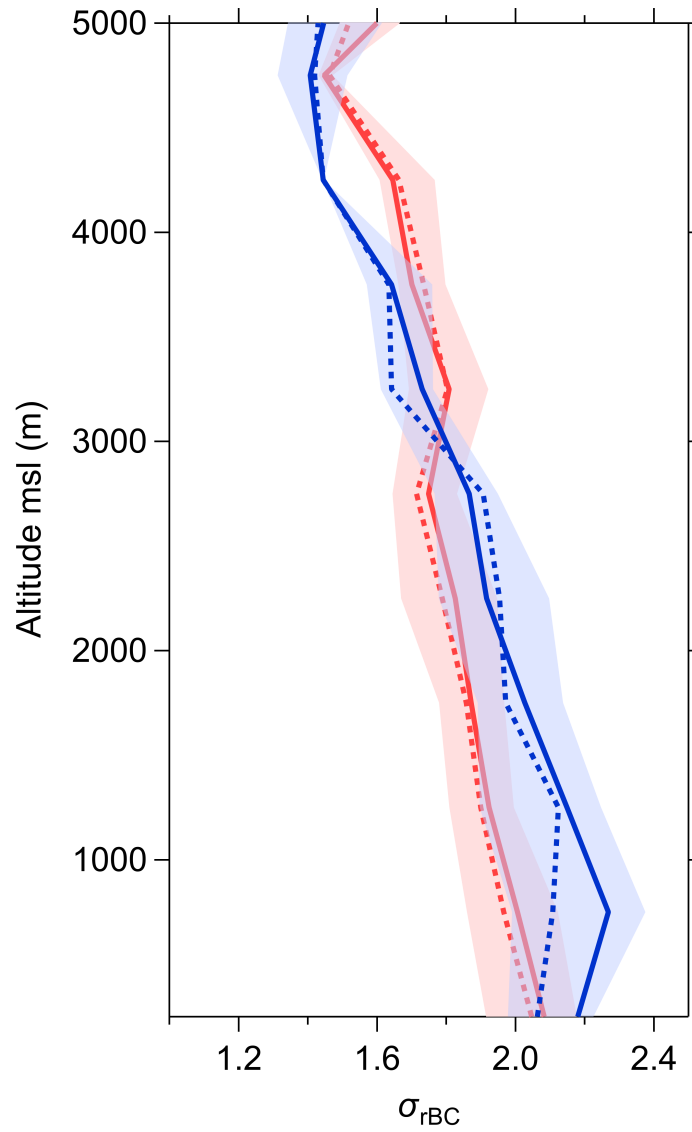
Figure A8. Vertical profiles of M_{BC} microphysical properties, the geometric standard deviation (σ_{rBC}) of the core size distributions. 2020 BLUESKY measurements in blue and 2017 EMeRGe EU measurements in red. Dashed lines show the median, solid lines the mean concentration and shaded areas represent interquartile range for each altitude bin of $500\,\mathrm{m}$.
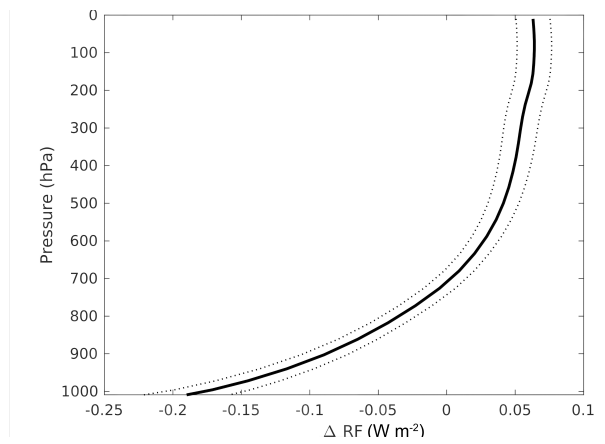
Figure A9. Profile for difference in aerosol radiative effect due to a reduction of 40% in M_{BC}. The profile is averaged for the months May and June over the region of HALO measurements (latitude between -5 and $16°$ and longitude between 37.5 and $54.5°$, Fig. 1).
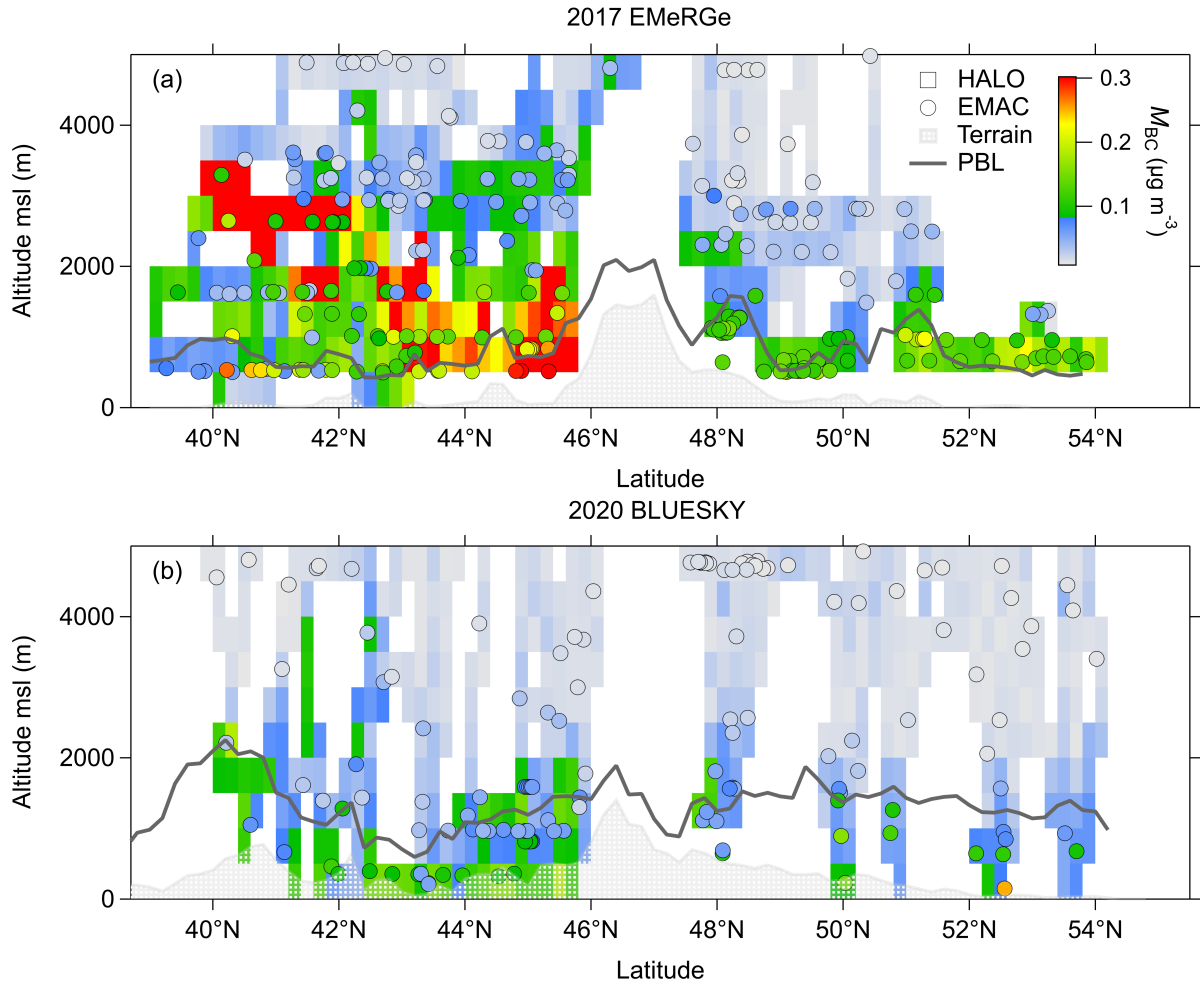
Figure A10. (a) Cross section of M_{BC} for 2017 EMeRGe EU measurements (rectangle marker). Arithmetic mean for all measurement data falling into a grid point of $0.2°$ latitude and $500\,\text{m}$ altitude. The color scale ranges from 0 to $0.3\,\mu\text{g/m}^3$. Means exceeding this range are shown in red. As round marker EMAC model results are displayed without further modification. (b) as (a) but for the 2020 BLUESKY measurements. The grey shading is the mean terrain height below flight track and the grey solid line shows the planetary boundary layer height below flight track (details in section A6).
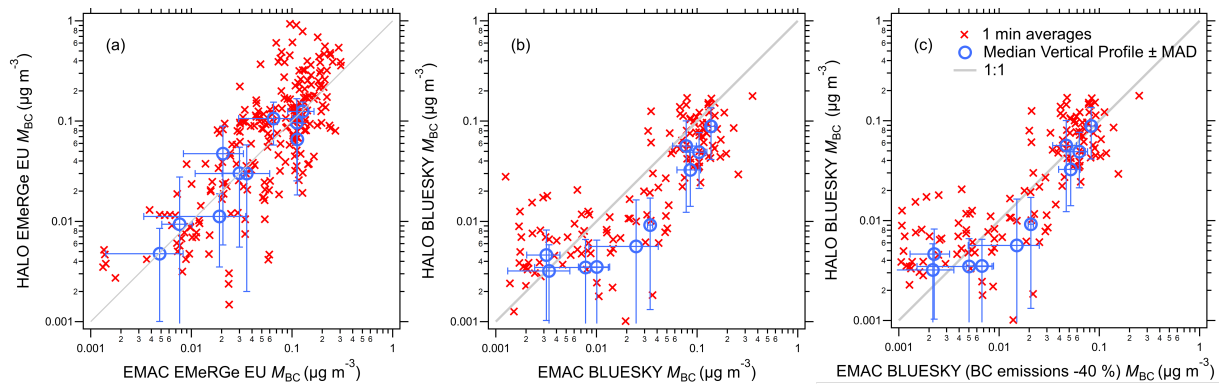
Figure A11. Scatter plot for median M_{BC} values of HALO measurements and EMAC model results. Red data shows the comparison of 1 minute averages. In blue median concentrations as used for the vertical profiles are shown. Error bars are one median absolute deviation (MAD) for the vertical merged data in 500 m altitude bins. Data shown is for the compared altitude up to 5000 m. (a) corresponds to measurements from 2017 with $R^2 = 0.76$. (b) are 2020 measurements with initial emissions in the EMAC model and $R^2 = 0.90$. (c) as (b) but with 40% reduced anthropogenic emissions in EMAC simulation and $R^2 = 0.90$.
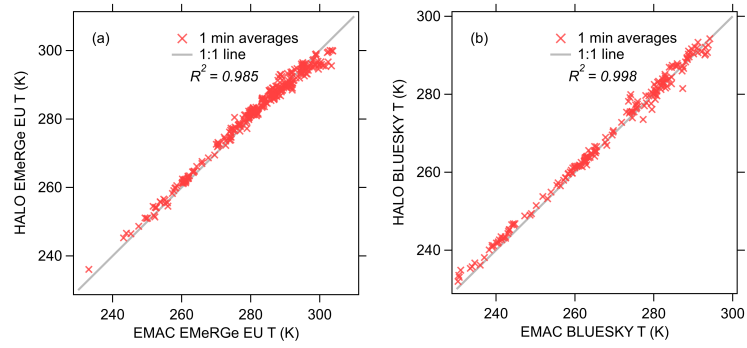
Figure A12. Scatter plot for ambient temperature (T) in K from HALO measurements and EMAC model simulations. Grey line is the one to one ratio. (a) corresponds to measurements from 2017 with R^2 = 0.985. (b) are 2020 measurements with R^2 = 0.998.
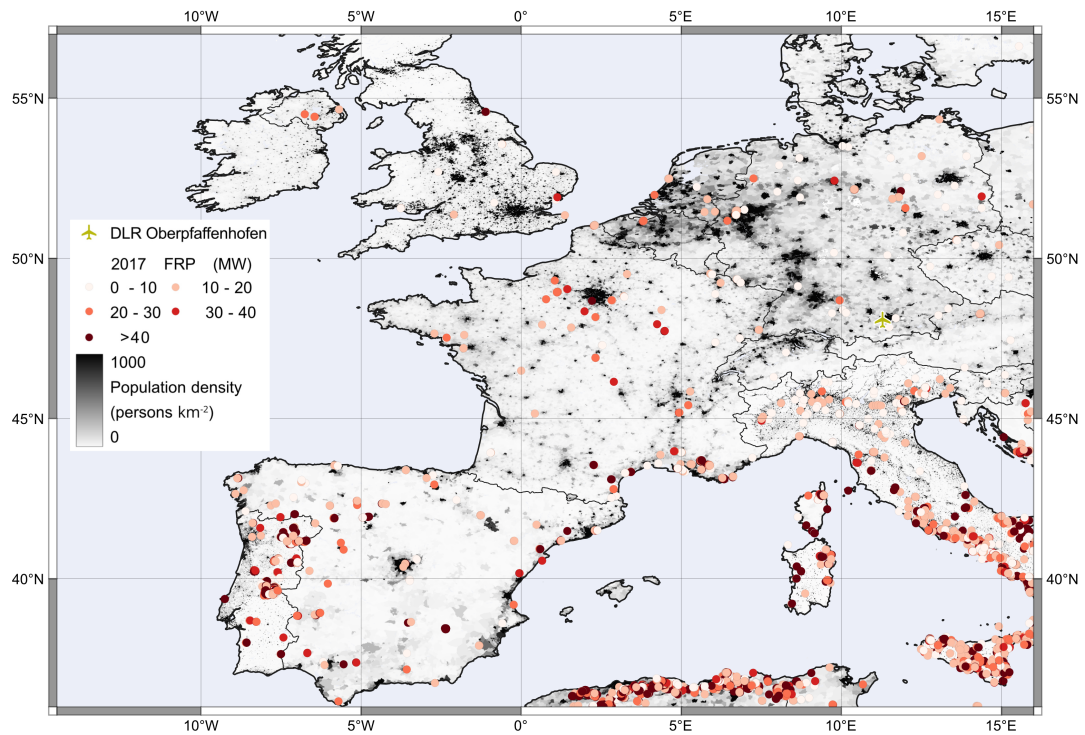
**Figure A13.** MODIS fires and thermal anomalies color-coded by Fire Radiative Power (FRP) in megawatts. Data was provided from https://firms.modaps.eosdis.nasa.gov/download/create.php, date of data downlaod 02.03.2022.
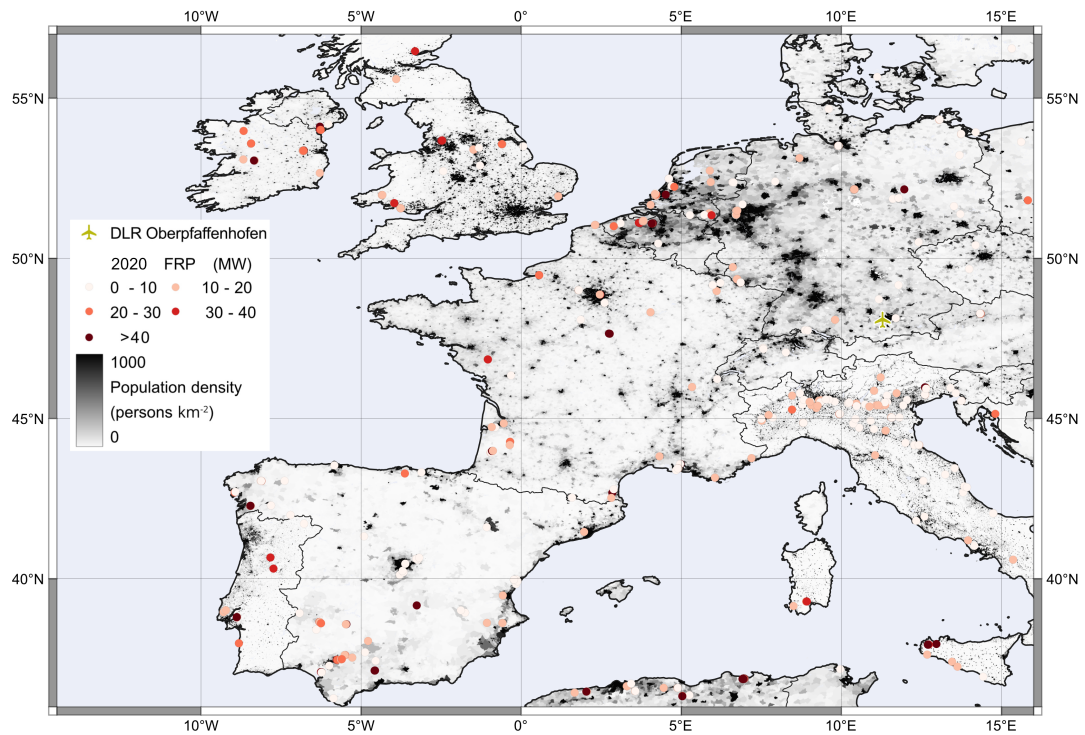
Figure A14. MODIS fires and thermal anomalies color-coded by Fire Radiative Power (FRP) in megawatts. Data was provided from https: //firms.modaps.eosdis.nasa.gov/download/create.php, date of data downlaod 02.03.2022.
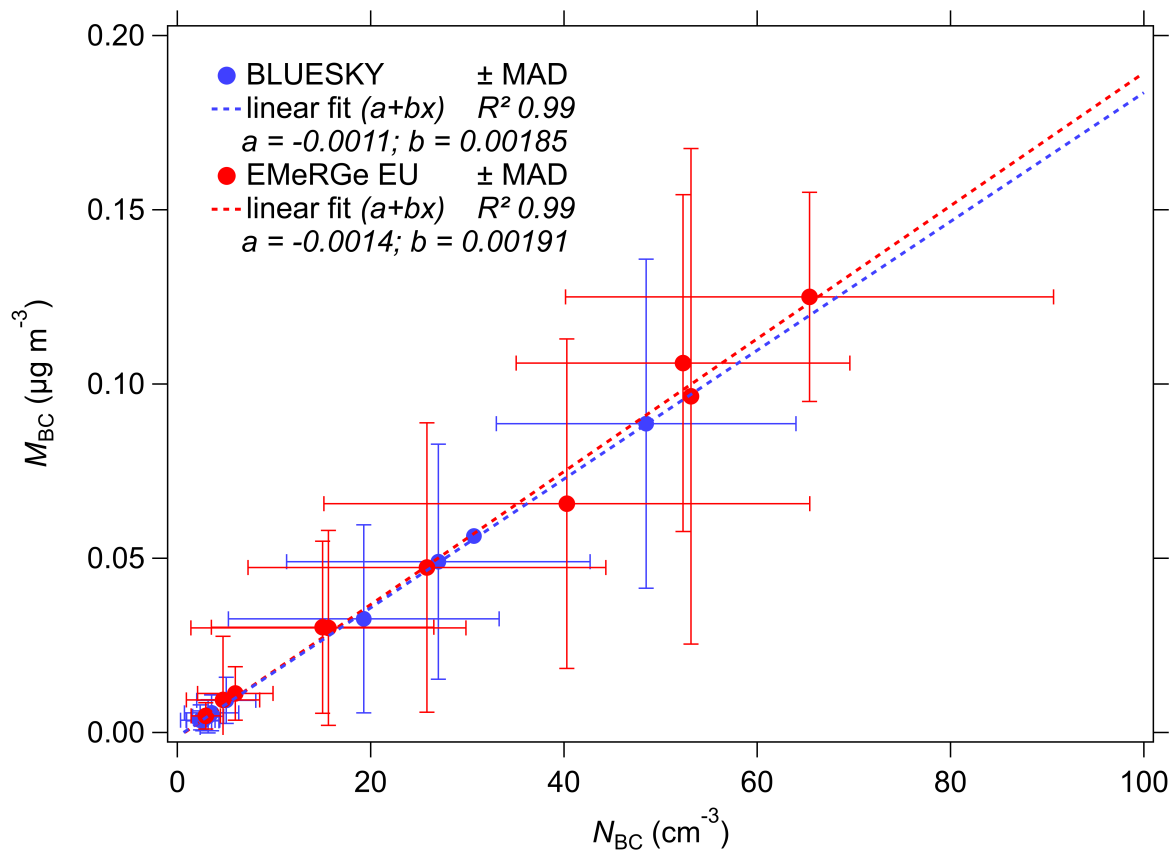
Figure A15. Scatter plot for data from vertical distribution of M_{BC} vs. N_{BC}. In red, data from 2017 collected during EMeRGe EU, in blue data from BLUESKY in 2020. Median absolute deviation (MAD) is shown as whiskers. Dashed lines are linear fits for each camapgin.

References

410 Andreae, M. O.: Aerosols Before Pollution, Science, 315, 50–51, https://doi.org/10.1126/science.1136529, 2007.

Andreae, M. O., Afchine, A., Albrecht, R., Holanda, B. A., Artaxo, P., Barbosa, H. M. J., Borrmann, S., Cecchini, M. A., Costa, A., Dollner, M., Fütterer, D., Järvinen, E., Jurkat, T., Klimach, T., Konemann, T., Knote, C., Krämer, M., Krisna, T., Machado, L. A. T., Mertes, S., Minikin, A., Pöhlker, C., Pöhlker, M. L., Pöschl, U., Rosenfeld, D., Sauer, D., Schlager, H., Schnaiter, M., Schneider, J., Schulz, C., Spanu, A., Sperling, V. B., Voigt, C., Walser, A., Wang, J., Weinzierl, B., Wendisch, M., and Ziereis, H.: Aerosol characteristics and particle pro-

415 duction in the upper troposphere over the Amazon Basin, Atmospheric Chemistry and Physics, 18, 921–961, https://doi.org/10.5194/acp-18-921-2018, https://www.atmos-chem-phys.net/18/921/2018/, 2018.

Andrés Hernández, M. D., Hilboll, A., Ziereis, H., Förster, E., Krüger, O. O., Kaiser, K., Schneider, J., Barnaba, F., Vrekoussis, M., Schmidt, J., Huntrieser, H., Blechschmidt, A.-M., George, M., Nenakhov, V., Klausner, T., Holanda, B. A., Wolf, J., Eirenschmalz, L., Krebsbach, M., Pöhlker, M. L., Hedegaard, A. B., Mei, L., Pfeilsticker, K., Liu, Y., Koppmann, R., Schlager, H., Bohn, B., Schumann, U., Richter, A.,

420 Schreiner, B., Sauer, D., Baumann, R., Mertens, M., Jöckel, P., Kilian, M., Stratmann, G., Pöhlker, C., Campanelli, M., Pandolfi, M., Sicard, M., Gomez-Amo, J. L., Pujadas, M., Bigge, K., Kluge, F., Schwarz, A., Daskalakis, N., Walter, D., Zahn, A., Pöschl, U., Bönisch, H., Borrmann, S., Platt, U., and Burrows, J. P.: Overview: On the transport and transformation of pollutants in the outflow of major population centres – observational data from the EMeRGe European intensive operational period in summer 2017, Atmospheric Chemistry and Physics Discussions, 2021, 1–81, https://doi.org/10.5194/acp-2021-500, https://acp.copernicus.org/preprints/acp-2021-500/, 2021.

425 Ban-Weiss, G. A., McLaughlin, J. P., Harley, R. A., Lunden, M. M., Kirchstetter, T. W., Kean, A. J., Strawa, A. W., Stevenson, E. D., and Kendall, G. R.: Long-term changes in emissions of nitrogen oxides and particulate matter from on-road gasoline and diesel vehicles, Atmospheric Environment, 42, 220–232, https://doi.org/10.1016/j.atmosenv.2007.09.049, 2008.

Ban-Weiss, G. A., Lunden, M. M., Kirchstetter, T. W., and Harley, R. A.: Measurement of black carbon and particle number emission factors from individual heavy-duty trucks, Environmental Science and Technology, 43, 1419–1424, https://doi.org/10.1021/es8021039, 2009.

430 Beer, C. G., Hendricks, J., Righi, M., Heinold, B., Tegen, I., Groß, S., Sauer, D., Walser, A., and Weinzierl, B.: Modelling mineral dust emissions and atmospheric dispersion with MADE3 in EMAC v2.54, Geosci. Model Dev., 13, 4287–4303, https://doi.org/10.5194/gmd-13-4287-2020, 2020.

Bond, T. C., Doherty, S. J., Fahey, D. W., Forster, P. M., Berntsen, T., Deangelo, B. J., Flanner, M. G., Ghan, S., Kärcher, B., Koch, D., Kinne, S., Kondo, Y., Quinn, P. K., Sarofim, M. C., Schultz, M. G., Schulz, M., Venkataraman, C., Zhang, H., Zhang, S., Bellouin, N.,

435 Guttikunda, S. K., Hopke, P. K., Jacobson, M. Z., Kaiser, J. W., Klimont, Z., Lohmann, U., Schwarz, J. P., Shindell, D., Storelvmo, T., Warren, S. G., and Zender, C. S.: Bounding the role of black carbon in the climate system: A scientific assessment, Journal of Geophysical Research Atmospheres, 118, 5380–5552, https://doi.org/10.1002/jgrd.50171, 2013.

Brühl, C., Lelieveld, J., Tost, H., Höpfner, M., and Glatthor, N.: Stratospheric sulfur and its implications for radiative forcing simulated by the chemistry climate model EMAC, J Geophys Res Atmos, 120, 2103–2118, https://doi.org/10.1002/2014JD022430, 2015.

440 CIESIN: Center for International Earth Science Information Network - CIESIN - Columbia University. 2018. Gridded Population of the World, Version 4 (GPWv4): Population Density, Revision 11. Palisades, NY: NASA Socioeconomic Data and Applications Center (SEDAC). Accessed 24 October 2021., https://doi.org/10.7927/H49C6VHW, 2018.

Dietmüller, S., Jöckel, P., Tost, H., Kunze, M., Gellhorn, C., Brinkop, S., Frömming, C., Ponater, M., Steil, B., Lauer, A., and Hendricks, J.: A new radiation infrastructure for the Modular Earth Submodel System (MESSy, based on version 2.51), Geosci Model Dev, 9, 2209–2222,

445 https://doi.org/10.5194/gmd-9-2209-2016, 2016.

Ding, S., Liu, D., Zhao, D., Hu, K., Tian, P., Zhou, W., Huang, M., Yang, Y., Wang, F., Sheng, J., Liu, Q., Kong, S., Cui, P., Huang, Y., He, H., Coe, H., and Ding, D.: Size-Related Physical Properties of Black Carbon in the Lower Atmosphere over Beijing and Europe, Environmental Science and Technology, 53, 11 112–11 121, https://doi.org/10.1021/acs.est.9b03722, 2019.

Ditas, J., Ma, N., Zhang, Y., Assmann, D., Neumaier, M., Riede, H., Karu, E., Williams, J., Scharffe, D., Wang, Q., Saturno, J., Schwarz, J. P., Katich, J. M., McMeeking, G. R., Zahn, A., Hermann, M., Brenninkmeijer, C. A. M., Andreae, M. O., Pöschl, U., Su, H., and Cheng, Y.: Strong impact of wildfires on the abundance and aging of black carbon in the lowermost stratosphere, Proceedings of the National Academy of Sciences, 115, E11 595–E11 603, https://doi.org/10.1073/pnas.1806868115, https://www.pnas.org/content/115/50/E11595, 2018.

Evangeliou, N., Platt, S. M., Eckhardt, S., Lund Myhre, C., Laj, P., Alados-Arboledas, L., Backman, J., Brem, B. T., Fiebig, M., Flentje, H., Marinoni, A., Pandolfi, M., Yus-Dìez, J., Prats, N., Putaud, J. P., Sellegri, K., Sorribas, M., Eleftheriadis, K., Vratolis, S., Wiedensohler, A., and Stohl, A.: Changes in black carbon emissions over Europe due to COVID-19 lockdowns, Atmospheric Chemistry and Physics, 21, 2675–2692, https://doi.org/10.5194/acp-21-2675-2021, 2021.

Forster, P. M., Forster, H. I., Evans, M. J., Gidden, M. J., Jones, C. D., Keller, C. A., Lamboll, R. D., Quéré, C. L., Rogelj, J., Rosen, D., Schleussner, C. F., Richardson, T. B., Smith, C. J., and Turnock, S. T.: Current and future global climate impacts resulting from COVID-19, Nature Climate Change, 10, 913–919, https://doi.org/10.1038/s41558-020-0883-0, 2020.

Goecke, H., Puls, T., and Wendt, J.: Vollbremsung: Die Folgen vonCorona für den Straßenverkehr, IW-Kurzbericht, 60, https://www.iwkoeln.de/fileadmin/user_upload/Studien/Kurzberichte/PDF/2020/IW-Kurzbericht_2020_Corona_Stra%C3%9Fenverkehr.pdf, 2020.

Gustafsson, Ö. and Ramanathan, V.: Convergence on climate warming by black carbon aerosols, Proceedings of the National Academy of Sciences of the United States of America, 113, 4243–4245, https://doi.org/10.1073/pnas.1603570113, 2016.

Gysel-Beer, M. and Corbin, J.: SP2 toolkit 4.115 (Igor7) (Version 4.115), http://doi.org/10.5281/zenodo.3575186/, 2019.

Hale, T., Angrist, N., Goldszmidt, R., Kira, B., Petherick, A., Phillips, T., Webster, S., Cameron-Blake, E., Hallas, L., Majumdar, S., and Tatlow, H.: A global panel database of pandemic policies (Oxford COVID-19 Government Response Tracker), Nature Human Behaviour, 5, 529–538, https://doi.org/10.1038/s41562-021-01079-8, http://dx.doi.org/10.1038/s41562-021-01079-8, 2021.

Heald, C. L., Ridley, D. A., Kroll, J. H., Barrett, S. R., Cady-Pereira, K. E., Alvarado, M. J., and Holmes, C. D.: Contrasting the direct radiative effect and direct radiative forcing of aerosols, Atmospheric Chemistry and Physics, 14, 5513–5527, https://doi.org/10.5194/acp-14-5513-2014, 2014.

Heintzenberg, J.: Properties of the log-normal particle size distribution, Aerosol Science and Technology, 21, 46–48, https://doi.org/10.1080/02786829408959695, 1994.

Hoesly, R. M., Smith, S. J., Feng, L., Klimont, Z., Janssens-Maenhout, G., Pitkanen, T., Seibert, J. J., Vu, L., Andres, R. J., Bolt, R. M., Bond, T. C., Dawidowski, L., Kholod, N., Kurokawa, J.-i., Li, M., Liu, L., Lu, Z., Moura, M. C. P., O'Rourke, P. R., and Zhang, Q.: Historical (1750–2014) anthropogenic emissions of reactive gases and aerosols from the Community Emissions Data System (CEDS), Geosci. Model Dev., 11, 369–408, https://doi.org/10.5194/gmd-11-369-2018, 2018.

Holanda, B. A., Pöhlker, M. L., Walter, D., Saturno, J., Sörgel, M., Ditas, J., Ditas, F., Schulz, C., Aurélio Franco, M., Wang, Q., Donth, T., Artaxo, P., Barbosa, H. M., Borrmann, S., Braga, R., Brito, J., Cheng, Y., Dollner, M., Kaiser, J. W., Klimach, T., Knote, C., Krüger, O. O., Fütterer, D., t.V. Lavric, J., Ma, N., MacHado, L. A., Ming, J., Morais, F. G., Paulsen, H., Sauer, D., Schlager, H., Schneider, J., Su, H., Weinzierl, B., Walser, A., Wendisch, M., Ziereis, H., Zöger, M., Pöschl, U., Andreae, M. O., and Pöhlker, C.: Influx of African biomass burning aerosol during the Amazonian dry season through layered transatlantic transport of black carbon-rich smoke, Atmospheric Chemistry and Physics, 20, 4757–4785, https://doi.org/10.5194/acp-20-4757-2020, 2020.

Jöckel, P., Sander, R., Kerkweg, A., Tost, H., and Lelieveld, J.: Technical Note: The Modular Earth Submodel System (MESSy) - a new approach towards Earth System Modeling, Atmos. Chem. Phys., 5, 433–444, https://doi.org/10.5194/acp-5-433-2005, 2005.

Jöckel, P., Kerkweg, A., Pozzer, A., Sander, R., Tost, H., Riede, H., Baumgaertner, A., Gromov, S., and Kern, B.: Development cycle 2 of the Modular Earth Submodel System (MESSy2), Geosci. Model Dev., 3, 717–752, https://doi.org/10.5194/gmd-3-717-2010, 2010.

Kaiser, J. W., Heil, A., Andreae, M. O., Benedetti, A., Chubarova, N., Jones, L., Morcrette, J.-J., Razinger, M., Schultz, M. G., Suttie, M., and van der Werf, G. R.: Biomass burning emissions estimated with a global fire assimilation system based on observed fire radiative power, Biogeosciences, 9, 527–554, https://doi.org/10.5194/bg-9-527-2012, 2012.

Kerkweg, A., Sander, R., Tost, H., and Jöckel, P.: Technical note: Implementation of prescribed (OFFLEM), calculated (ONLEM), and pseudo-emissions (TNUDGE) of chemical species in the Modular Earth Submodel System (MESSy), Atmos. Chem. Phys., 6, 3603–3609, https://doi.org/10.5194/acp-6-3603-2006, 2006.

Ketzel, M. and Berkowicz, R.: Modelling the fate of ultrafine particles from exhaust pipe to rural background: an analysis of time scales for dilution, coagulation and deposition, Atmospheric Environment, 38, 2639–2652, https://doi.org/https://doi.org/10.1016/j.atmosenv.2004.02.020, https://www.sciencedirect.com/science/article/pii/S1352231004001724, 2004.

Klingmüller, K., Lelieveld, J., Karydis, V. A., and Stenchikov, G. L.: Direct radiative effect of dust–pollution interactions, Atmos Chem Phys, 19, 7397–7408, https://doi.org/10.5194/acp-19-7397-2019, 2019.

Kutzner, R. D., von Schneidemesser, E., Kuik, F., Quedenau, J., Weatherhead, E. C., and Schmale, J.: Long-term monitoring of black carbon across Germany, Atmospheric Environment, 185, 41–52, https://doi.org/https://doi.org/10.1016/j.atmosenv.2018.04.039, https://www.sciencedirect.com/science/article/pii/S135223101830270X, 2018.

Laborde, M., Schnaiter, M., Linke, C., Saathoff, H., Naumann, K.-H., Möhler, O., Berlenz, S., Wagner, U., Taylor, J. W., Liu, D., Flynn, M., Allan, J. D., Coe, H., Heimerl, K., Dahlkötter, F., Weinzierl, B., Wollny, A. G., Zanatta, M., Cozic, J., Laj, P., Hitzenberger, R., Schwarz, J. P., and Gysel, M.: Single Particle Soot Photometer intercomparison at the AIDA chamber, Atmospheric Measurement Techniques, 5, 3077–3097, https://doi.org/10.5194/amt-5-3077-2012, 2012.

Laborde, M., Crippa, M., Tritscher, T., Jurányi, Z., Decarlo, P. F., Temime-Roussel, B., Marchand, N., Eckhardt, S., Stohl, A., Baltensperger, U., Prévôt, A. S., Weingartner, E., and Gysel, M.: Black carbon physical properties and mixing state in the European megacity Paris, Atmospheric Chemistry and Physics, 13, 5831–5856, https://doi.org/10.5194/acp-13-5831-2013, 2013.

Lauer, A., Eyring, V., Hendricks, J., Jöckel, P., and Lohmann, U.: Global model simulations of the impact of ocean-going ships on aerosols, clouds, and the radiation budget, Atmos Chem Phys, 7, 5061–5079, https://doi.org/10.5194/acp-7-5061-2007, 2007.

Le Quéré, C., Jackson, R. B., Jones, M. W., Smith, A. J., Abernethy, S., Andrew, R. M., De-Gol, A. J., Willis, D. R., Shan, Y., Canadell, J. G., Friedlingstein, P., Creutzig, F., and Peters, G. P.: Temporary reduction in daily global CO2 emissions during the COVID-19 forced confinement, Nature Climate Change, 10, 647–653, https://doi.org/10.1038/s41558-020-0797-x, http://dx.doi.org/10.1038/s41558-020-0797-x, 2020.

Lelieveld, J., Brühl, C., Jöckel, P., Steil, B., Crutzen, P. J., Fischer, H., Giorgetta, M. A., Hoor, P., Lawrence, M. G., Sausen, R., and Tost, H.: Stratospheric dryness: model simulations and satellite observations, Atmos Chem Phys, 7, 1313–1332, https://doi.org/10.5194/acp-7-1313-2007, 2007.

Lelieveld, J., Klingmueller, K., Pozzer, A., Burnett, R. T., Haines, A., and Ramanathan, V.: Effects of fossil fuel and total anthropogenic emission removal on public health and climate, Proc Natl Acad Sci U.S.A, 116, 7192–7197, https://doi.org/10.1073/pnas.1819989116, 2019.

Li, Q. and Groß, S.: Changes of cirrus cloud properties and occurrence over Europe during the COVID-19 caused air traffic reduction, Atmospheric Chemistry and Physics Discussions, pp. 1–25, https://doi.org/10.5194/acp-2021-172, 2021.

Liu, D., Allan, J. D., Young, D. E., Coe, H., Beddows, D., Fleming, Z. L., Flynn, M. J., Gallagher, M. W., Harrison, R. M., Lee, J., Prevot, A. S., Taylor, J. W., Yin, J., Williams, P. I., and Zotter, P.: Size distribution, mixing state and source apportionment of black carbon aerosol in London during winter time, Atmospheric Chemistry and Physics, 14, 10 061–10 084, https://doi.org/10.5194/acp-14-10061-2014, 2014.

Liu, D., Ding, S., Zhao, D., Hu, K., Yu, C., Hu, D., Wu, Y., Zhou, C., Tian, P., Liu, Q., Wu, Y., Zhang, J., Kong, S., Huang, M., and Ding, D.: Black Carbon Emission and Wet Scavenging From Surface to the Top of Boundary Layer Over Beijing Region, Journal of Geophysical Research: Atmospheres, 125, 1–15, https://doi.org/10.1029/2020JD033096, 2020.

Lonati, G. and Riva, F.: Regional scale impact of the covid-19 lockdown on air quality: Gaseous pollutants in the po valley, northern Italy, Atmosphere, 12, https://doi.org/10.3390/atmos12020264, 2021.

Lund, M. T., Samset, B. H., Skeie, R. B., Watson-Parris, D., Katich, J. M., Schwarz, J. P., and Weinzierl, B.: Short Black Carbon lifetime inferred from a global set of aircraft observations, npj Climate and Atmospheric Science, 1, 1–8, https://doi.org/10.1038/s41612-018-0040-x, http://dx.doi.org/10.1038/s41612-018-0040-x, 2018.

McDuffie, E. E., Smith, S. J., O'Rourke, P., Tibrewal, K., Venkataraman, C., Marais, E. A., Zheng, B., Crippa, M., Brauer, M., and Martin, R. V.: A global anthropogenic emission inventory of atmospheric pollutants from sector- and fuel-specific sources (1970–2017): an application of the Community Emissions Data System (CEDS), Earth System Science Data, 12, 3413–3442, https://doi.org/10.5194/essd-12-3413-2020, https://essd.copernicus.org/articles/12/3413/2020/, 2020.

Moreda-Piñeiro, J., Sánchez-Piñero, J., Fernández-Amado, M., Costa-Tomé, P., Gallego-Fernández, N., Piñeiro-Iglesias, M., López-Mahía, P., and Muniategui-Lorenzo, S.: Evolution of gaseous and particulate pollutants in the air: What changed after five lockdown weeks at a southwest atlantic european region (northwest of spain) due to the sars-cov-2 pandemic?, Atmosphere, 12, https://doi.org/10.3390/atmos12050562, 2021.

Naik, V., Szopa, S., Adhikary, B., Artaxo, P., Berntsen, T., Collins, W. D., Fuzzi, S., Gallardo, L., Kiendler Scharr, A., Klimont, Z., Liao, H., Unger, N., and Zanis, P.: Climate Change 2021: The Physical Science Basis. Contribution of Working Group I to the Sixth Assessment Report of the Intergovernmental Panel on Climate Change, Cambridge University Press, 2021. In Press.

Ohata, S., Moteki, N., Mori, T., Koike, M., and Kondo, Y.: A key process controlling the wet removal of aerosols: New observational evidence, Scientific Reports, 6, 1–9, https://doi.org/10.1038/srep34113, 2016.

Paasonen, P., Kupiainen, K., Klimont, Z., Visschedijk, A., Denier van der Gon, H. A. C., and Amann, M.: Continental anthropogenic primary particle number emissions, Atmos. Chem. Phys., 16, 6823–6840, https://doi.org/10.5194/acp-16-6823-2016, 2016.

Peitzmeier, C., Loschke, C., Wiedenhaus, H., and Klemm, O.: Real-world vehicle emissions as measured by in situ analysis of exhaust plumes, Environmental Science and Pollution Research, 24, 23 279–23 289, https://doi.org/10.1007/s11356-017-9941-1, 2017.

Petetin, H., Bowdalo, D., Soret, A., Guevara, M., Jorba, O., Serradell, K., and Pérez García-Pando, C.: Meteorology-normalized impact of the COVID-19 lockdown upon NO2 pollution in Spain, Atmospheric Chemistry and Physics, 20, 11 119–11 141, https://doi.org/10.5194/acp-20-11119-2020, 2020.

Pileci, R. E., Modini, R. L., Bertò, M., Yuan, J., Corbin, J. C., Marinoni, A., Henzing, B., Moerman, M. M., Putaud, J. P., Spindler, G., Wehner, B., Müller, T., Tuch, T., Trentini, A., Zanatta, M., Baltensperger, U., and Gysel-Beer, M.: Comparison of co-located refractory black carbon (rBC) and elemental carbon (EC) mass concentration measurements during field campaigns at several European sites, Atmospheric Measurement Techniques, 14, 1379–1403, https://doi.org/10.5194/amt-14-1379-2021, https://amt.copernicus.org/articles/14/1379/2021/, 2021.

560 Pohjola, M., Pirjola, L., Kukkonen, J., and Kulmala, M.: Modelling of the influence of aerosol processes for the dispersion of vehicular exhaust plumes in street environment, Atmospheric Environment, 37, 339–351, https://doi.org/https://doi.org/10.1016/S1352-2310(02)00887-7, https://www.sciencedirect.com/science/article/pii/S1352231002008877, 2003.

Pöschl, U.: Atmospheric aerosols: Composition, transformation, climate and health effects, Angewandte Chemie - International Edition, 44, 7520–7540, https://doi.org/10.1002/anie.200501122, 2005.

565 Pozzer, A., de Meij, A., Pringle, K. J., Tost, H., Doering, U. M., van Aardenne, J., and Lelieveld, J.: Distributions and regional budgets of aerosols and their precursors simulated with the EMAC chemistry-climate model, Atmos. Chem. Phys., 12, 961–987, https://doi.org/10.5194/acp-12-961-2012, 2012.

Pozzer, A., de Meij, A., Yoon, J., Tost, H., Georgoulias, A. K., and Astitha, M.: AOD trends during 2001–2010 from observations and model simulations, Atmos Chem Phys, 15, 5521–5535, https://doi.org/10.5194/acp-15-5521-2015, 2015.

570 Pringle, K. J., Tost, H., Message, S., Steil, B., Giannadaki, D., Nenes, A., Fountoukis, C., Stier, P., Vignati, E., and Lelieveld, J.: Description and evaluation of GMXe: a new aerosol submodel for global simulations (v1), Geosci. Model Dev., 3, 391–412, https://doi.org/10.5194/gmd-3-391-2010, 2010.

Quaas, M. F., Meya, J. N., Schenk, H., Bos, B., Drupp, M. A., and Requate, T.: The social cost of contacts: Theory and evidence for the first wave of the COVID-19 pandemic in Germany, PLOS ONE, 16, 1–29, https://doi.org/10.1371/journal.pone.0248288, https://doi.org/
575 10.1371/journal.pone.0248288, 2021a.

Quaas, M. F., Meya, J. N., Schenk, H., Bos, B., Drupp, M. A., and Requate, T.: The social cost of contacts: Theory and evidence for the first wave of the COVID-19 pandemic in Germany, PLOS ONE, 16, 1–29, https://doi.org/10.1371/journal.pone.0248288, https://doi.org/
10.1371/journal.pone.0248288, 2021b.

Querol, X., Alastuey, A., Viana, M., Moreno, T., Reche, C., Minguillón, M. C., Ripoll, A., Pandolfi, M., Amato, F., Karanasiou, A., Pérez, N.,
580 Pey, J., Cusack, M., Vázquez, R., Plana, F., Dall'Osto, M., de la Rosa, J., Sánchez de la Campa, A., Fernández-Camacho, R., Rodríguez, S., Pio, C., Alados-Arboledas, L., Titos, G., Artíñano, B., Salvador, P., García Dos Santos, S., and Fernández Patier, R.: Variability of carbonaceous aerosols in remote, rural, urban and industrial environments in Spain: implications for air quality policy, Atmospheric Chemistry and Physics, 13, 6185–6206, https://doi.org/10.5194/acp-13-6185-2013, https://acp.copernicus.org/articles/13/6185/2013/, 2013.

Ramanathan, V. and Carmichael, G.: Global and regional climate changes due to black carbon, Nature Geoscience, 1, 221–227,
585 https://doi.org/10.1038/ngeo156, 2008.

Reddington, C. L., McMeeking, G., Mann, G. W., Coe, H., Frontoso, M. G., Liu, D., Flynn, M., Spracklen, D. V., and Carslaw, K. S.: The mass and number size distributions of black carbon aerosol over Europe, Atmospheric Chemistry and Physics, 13, 4917–4939, https://doi.org/10.5194/acp-13-4917-2013, 2013.

Rolph, G., Stein, A., and Stunder, B.: Real-time Environmental Applications and Display sYstem: READY, Environmental Modelling and
590 Software, 95, 210–228, https://doi.org/10.1016/j.envsoft.2017.06.025, http://dx.doi.org/10.1016/j.envsoft.2017.06.025, 2017.

S. Raj, S., Krüger, O. O., Sharma, A., Panda, U., Pöhlker, C., Walter, D., Förster, J.-D., Singh, R. P., S., S., Klimach, T., Darbyshire, E., Martin, S. T., McFiggans, G., Coe, H., Allan, J., R., R., Soni, V. K., Su, H., Andreae, M. O., Pöschl, U., Pöhlker, M. L., and Gunthe, S. S.: Planetary Boundary Layer Height Modulates Aerosol—Water Vapor Interactions During Winter in the Megacity of Delhi, Journal of Geophysical Research: Atmospheres, 126, e2021JD035 681, https://doi.org/https://doi.org/10.1029/2021JD035681, https://agupubs.
595 onlinelibrary.wiley.com/doi/abs/10.1029/2021JD035681, e2021JD035681 2021JD035681, 2021.

Sander, R., Kerkweg, A., Jöckel, P., and Lelieveld, J.: Technical note: The new comprehensive atmospheric chemistry module MECCA, Atmos. Chem. Phys., 5, 445–450, https://doi.org/10.5194/acp-5-445-2005, 2005.

Sander, R., Baumgaertner, A., Cabrera-Perez, D., Frank, F., Gromov, S., Großß, J.-U., Harder, H., Huijnen, V., Jöckel, P., Karydis, V. A., Niemeyer, K. E., Pozzer, A., Riede, H., Schultz, M. G., Taraborrelli, D., and Tauer, S.: The community atmospheric chemistry box model CAABA/MECCA-4.0, Geosci. Model Dev., 12, 1365–1385, https://doi.org/10.5194/gmd-12-1365-2019, 2019.

Schumann, U., Bugliaro, L., Dörnbrack, A., Baumann, R., and Voigt, C.: Aviation Contrail Cirrus and Radiative Forcing Over Europe During 6 Months of COVID-19, Geophysical Research Letters, 48, e2021GL092 771, https://doi.org/https://doi.org/10.1029/2021GL092771, https://agupubs.onlinelibrary.wiley.com/doi/abs/10.1029/2021GL092771, e2021GL092771 2021GL092771, 2021a.

Schumann, U., Poll, I., Teoh, R., Koelle, R., Spinielli, E., Molloy, J., Koudis, G. S., Baumann, R., Bugliaro, L., Stettler, M., and Voigt, C.: Air traffic and contrail changes over Europe during COVID-19: a model study, Atmospheric Chemistry and Physics, 21, 7429–7450, https://doi.org/10.5194/acp-21-7429-2021, https://acp.copernicus.org/articles/21/7429/2021/, 2021b.

Schwarz, J. P., Gao, R. S., Fahey, D. W., Thomson, D. S., Watts, L. A., Wilson, J. C., Reeves, J. M., Darbeheshti, M., Baumgardner, D. G., Kok, G. L., Chung, S. H., Schulz, M., Hendricks, J., Lauer, A., Kärcher, B., Slowik, J. G., Rosenlof, K. H., Thompson, T. L., Langford, A. O., Loewenstein, M., and Aikin, K. C.: Single-particle measurements of midlatitude black carbon and light-scattering aerosols from the boundary layer to the lower stratosphere, Journal of Geophysical Research Atmospheres, 111, 1–15, https://doi.org/10.1029/2006JD007076, 2006.

Schwarz, J. P., Gao, R. S., Spackman, J. R., Watts, L. A., Thomson, D. S., Fahey, D. W., Ryerson, T. B., Peischl, J., Holloway, J. S., Trainer, M., Frost, G. J., Baynard, T., Lack, D. A., de Gouw, J. A., Warneke, C., and Del Negro, L. A.: Measurement of the mixing state, mass, and optical size of individual black carbon particles in urban and biomass burning emissions, Geophysical Research Letters, 35, 1–5, https://doi.org/10.1029/2008GL033968, 2008.

Schwarz, J. P., Weinzierl, B., Samset, B. H., Dollner, M., Heimerl, K., Markovic, M. Z., Perring, A. E., and Ziemba, L.: Aircraft measurements of black carbon vertical profiles show upper tropospheric variability and stability, Geophysical Research Letters, 44, 1132–1140, https://doi.org/https://doi.org/10.1002/2016GL071241, https://agupubs.onlinelibrary.wiley.com/doi/abs/10.1002/2016GL071241, 2017.

Seinfeld, J. H. and Pandis, S. N.: Atmospheric Chemistry and Physics: From Air Pollution to Climate Change, John Wiley & Sons, Inc., https://doi.org/10.1063/1.882420, 2006.

Shi, Z., Song, C., Liu, B., Lu, G., Xu, J., Van Vu, T., Elliott, R. J., Li, W., Bloss, W. J., and Harrison, R. M.: Abrupt but smaller than expected changes in surface air quality attributable to COVID-19 lockdowns, Science Advances, 7, https://doi.org/10.1126/sciadv.abd6696, 2021.

Singh, V., Ravindra, K., Sahu, L., and Sokhi, R.: Trends of atmospheric black carbon concentration over the United Kingdom, Atmospheric Environment, 178, 148–157, https://doi.org/https://doi.org/10.1016/j.atmosenv.2018.01.030, https://www.sciencedirect.com/science/article/pii/S135223101830044X, 2018.

Stein, A. F., Draxler, R. R., Rolph, G. D., Stunder, B. J., Cohen, M. D., and Ngan, F.: Noaa's hysplit atmospheric transport and dispersion modeling system, Bulletin of the American Meteorological Society, 96, 2059–2077, https://doi.org/10.1175/BAMS-D-14-00110.1, 2015.

Stephens, M., Turner, N., and Sandberg, J.: Particle identification by laser-induced incandescence in a solid-state laser cavity, Applied Optics, 42, 3726, https://doi.org/10.1364/ao.42.003726, 2003.

Tsimpidi, A. P., Karydis, V. A., Pozzer, A., Pandis, S. N., and Lelieveld, J.: ORACLE (v1.0): module to simulate the organic aerosol composition and evolution in the atmosphere, Geosci. Model Dev., 7, 3153–3172, https://doi.org/10.5194/gmd-7-3153-2014, 2014.

Tsimpidi, A. P., Karydis, V. A., Pozzer, A., Pandis, S. N., and Lelieveld, J.: ORACLE 2-D (v2.0): an efficient module to compute the volatility and oxygen content of organic aerosol with a global chemistry–climate model, Geosci. Model Dev., 11, 3369–3389, https://doi.org/10.5194/gmd-11-3369-2018, 2018.

Venter, Z. S., Aunan, K., Chowdhury, S., and Lelieveld, J.: COVID-19 lockdowns cause global air pollution declines, Proceedings of the National Academy of Sciences, 117, 18 984–18 990, https://doi.org/10.1073/pnas.2006853117, https://www.pnas.org/content/117/32/18984, 2020.

Vignati, E., Berkowicz, R., Palmgren, F., Lyck, E., and Hummelshøj, P.: Transformation of size distributions of emitted particles in streets, Science of The Total Environment, 235, 37–49, https://doi.org/https://doi.org/10.1016/S0048-9697(99)00188-6, https://www.sciencedirect.com/science/article/pii/S0048969799001886, 1999.

Voigt, C., Lelieveld, J., Schlager, H., Schneider, J., Curtius, J., Meerkötter, R., Sauer, D., Bugliaro, L., Bohn, B., Crowley, J. N., Erbertseder, T., Groβ, S., Hahn, V., Li, Q., Mertens, M., Pöhlker, M. L., Pozzer, A., Schumann, U., Tomsche, L., Williams, J., Zahn, A., Andreae, M., Borrmann, S., Bräuer, T., Dörich, R., Dörnbrack, A., Edtbauer, A., Ernle, L., Fischer, H., Giez, A., Granzin, M., Grewe, V., Harder, H., Heinritzi, M., Holanda, B. A., Jöckel, P., Kaiser, K., Krüger, O. O., Lucke, J., Marsing, A., Martin, A., Matthes, S., Pöhlker, C., Pöschl, U., Reifenberg, S., Ringsdorf, A., Scheibe, M., Tadic, I., Zauner-Wieczorek, M., Henke, R., and Rapp, M.: Cleaner skies during the COVID-19 lockdown, Bulletin of the American Meteorological Society, pp. 1–57, https://doi.org/10.1175/bams-d-21-0012.1, 2022.

Wiesner, A., Pfeifer, S., Merkel, M., Tuch, T., Weinhold, K., and Wiedensohler, A.: Real world vehicle emission factors for black carbon derived from longterm in-situ measurements and inverse modelling, Atmosphere, 12, 1–19, https://doi.org/10.3390/atmos12010031, 2021.

Wren, S. N., Liggio, J., Han, Y., Hayden, K., Lu, G., Mihele, C. M., Mittermeier, R. L., Stroud, C., Wentzell, J. J., and Brook, J. R.: Elucidating real-world vehicle emission factors from mobile measurements over a large metropolitan region: A focus on isocyanic acid, hydrogen cyanide, and black carbon, Atmospheric Chemistry and Physics, 18, 16 979–17 001, https://doi.org/10.5194/acp-18-16979-2018, 2018.

Zimmermann, P. H., Brenninkmeijer, C. A. M., Pozzer, A., Jöckel, P., Winterstein, F., Zahn, A., Houweling, S., and Lelieveld, J.: Model simulations of atmospheric methane (1997–2016) and their evaluation using NOAA and AGAGE surface and IAGOS-CARIBIC aircraft observations, Atmos Chem Phys, 20, 5787–5809, https://doi.org/10.5194/acp-20-5787-2020, 2020.